

GUIDELINES

Magnetic Resonance in Medicine

Recommendations for quantitative cerebral perfusion MRI using multi-timepoint arterial spin labeling: Acquisition, quantification, and clinical applications

Joseph G. Woods^{1,2}  | Eric Achten³  | Iris Asllani^{4,5} | Divya S. Bolar²  |
 Weiying Dai⁶ | John A. Detre⁷ | Audrey P. Fan^{8,9} |
 María A. Fernández-Seara^{10,11}  | Xavier Golay^{12,13}  | Matthias Günther^{14,15} |
 Jia Guo¹⁶  | Luis Hernandez-Garcia¹⁷  | Mai-Lan Ho¹⁸  |
 Meher R. Juttukonda^{19,20}  | Hanzhang Lu²¹  | Bradley J. MacIntosh^{22,23,24}  |
 Ananth J. Madhuranthakam²⁵  | Henk-Jan Mutsaerts^{26,27}  |
 Thomas W. Okell¹  | Laura M. Parkes^{28,29}  | Nandor Pinter^{30,31}  | Joana Pinto³²  |
 Qin Qin²¹  | Marion Smits^{33,34,35}  | Yuriko Suzuki¹  | David L. Thomas³⁶  |
 Matthias J. P. Van Osch³⁷  | Danny J. J. Wang³⁸  | Esther A. H. Warnert^{33,35}  |
 Greg Zaharchuk³⁹ | Fernando Zelaya⁴⁰ | Moss Zhao^{39,41}  | Michael A. Chappell^{1,42}  |
 on behalf of the ISMRM Perfusion Study Group

Correspondence

Joseph G. Woods, Wellcome Centre for Integrative Neuroimaging, FMRIB, Nuffield Department of Clinical Neurosciences, University of Oxford, Oxford, UK.
 Email: joseph.woods@ndcn.ox.ac.uk

Funding information

Spanish Ministry of Science and Innovation, Grant/Award Number: PI21/00578; National Institutes of Health, Grant/Award Number: R01-EB025220; Nederlandse Organisatie voor Wetenschappelijk Onderzoek, Grant/Award Number: 016.160.351; Engineering and Physical Sciences Research Council, Grant/Award Number: EP/S021507/1; National Cancer Institute, Grant/Award Number: U01 CA207091; National Institute on Aging, Grant/Award Number: K01-AG070318; National Institute of Neurological Disorders and

Abstract

Accurate assessment of cerebral perfusion is vital for understanding the hemodynamic processes involved in various neurological disorders and guiding clinical decision-making. This guidelines article provides a comprehensive overview of quantitative perfusion imaging of the brain using multi-timepoint arterial spin labeling (ASL), along with recommendations for its acquisition and quantification. A major benefit of acquiring ASL data with multiple label durations and/or post-labeling delays (PLDs) is being able to account for the effect of variable arterial transit time (ATT) on quantitative perfusion values and additionally visualize the spatial pattern of ATT itself, providing valuable clinical insights. Although multi-timepoint data can be acquired in the same scan time as single-PLD data with comparable perfusion measurement precision, its acquisition and postprocessing presents challenges beyond single-PLD ASL, impeding widespread adoption. Building upon the 2015 ASL consensus article, this work highlights the protocol distinctions specific to multi-timepoint ASL and provides robust recommendations for acquiring high-quality data.

For affiliations refer to page 486

This is an open access article under the terms of the [Creative Commons Attribution](https://creativecommons.org/licenses/by/4.0/) License, which permits use, distribution and reproduction in any medium, provided the original work is properly cited.

© 2024 The Authors. *Magnetic Resonance in Medicine* published by Wiley Periodicals LLC on behalf of International Society for Magnetic Resonance in Medicine.

Stroke, Grant/Award Numbers: R00-NS-102884, R01-NS123025; Wellcome Trust, Grant/Award Numbers: 220204/Z/20/Z, 203139/Z/16/Z, 539208; National Institute of Biomedical Imaging and Bioengineering, Grant/Award Number: R01EB033210

Additionally, we propose an extended quantification model based on the 2015 consensus model and discuss relevant postprocessing options to enhance the analysis of multi-timepoint ASL data. Furthermore, we review the potential clinical applications where multi-timepoint ASL is expected to offer significant benefits. This article is part of a series published by the International Society for Magnetic Resonance in Medicine (ISMRM) Perfusion Study Group, aiming to guide and inspire the advancement and utilization of ASL beyond the scope of the 2015 consensus article.

KEYWORDS

arterial spin labeling, arterial transit time, cerebral blood flow, multi-timepoint, perfusion

1 | INTRODUCTION

Arterial spin labeling (ASL) perfusion MRI is a non-invasive technique to quantitatively map the supply of blood to an organ. Given the critical role perfusion plays in nutrient delivery, the ability to quantitatively map perfusion has an important role in the diagnosis and monitoring of a wide variety of diseases. The major MRI platforms now all have ASL sequences capable of obtaining high-quality whole-brain perfusion images within a few minutes of scanning. ASL has been validated against exogenous contrast enhanced perfusion MRI^{1–4} and PET,^{5–11} has been demonstrated to be reproducible in multi-center studies,^{12,13} and has been increasingly deployed in clinical settings.^{14–19}

To achieve simple, robust perfusion quantification, the consensus recommendation, published in 2015,²⁰ was to perform repeated acquisitions using a fixed label duration (LD) and single post-labeling delay (PLD)ⁱ; the resulting data being averaged to achieve sufficient SNR for interpretation. An acknowledged limitation of this approach is potential sensitivity to variation in the time it takes for blood to travel from the labeling region to the tissue in each voxel, known as the arterial transit time (ATT). The recommendations controlled for this by recommending a combination of LD and PLD that would be largely insensitive to ATT except where it is prolonged beyond a typical range; formally, single-PLD ASL will be relatively insensitive to ATT when the PLD used is longer than the ATT.²³

An alternative approach, also discussed in the 2015 consensus paper, is the use of multi-PLD/multi-timepoint ASL.^{23–28} In this case, the time-based parameters of LD and/or PLD are varied over repeated acquisitions. The resulting data can be combined via kinetic modeling to produce estimates of both cerebral blood flow (CBF) and ATT, with the estimated CBF being inherently insensitive to variation in ATT (see Figure 1).^{29,30} This is particularly relevant in settings where the ATT deviates substantially

from normal, for example, in steno-occlusive diseases (see Figure 2),^{33,34} or is variable between individuals or conditions, for example, in cerebrovascular reactivity (CVR) studies.¹¹ ATT has also been shown to be a useful physiological marker of disease in and of itself.^{35–44} Finally, multi-timepoint ASL offers the opportunity to extract quantitative maps of additional hemodynamic parameters.^{45–48}

The 2015 single-PLD consensus²⁰ still represents the recommended clinical ASL implementation due to its simplicity and ease of use. However, there has been continued technical development alongside substantial growth in the use of ASL and understanding of how to deploy it in research and clinical practice since that time. Therefore, we believe it is timely to offer specific recommendations for situations where quantitative perfusion metrics derived from multi-timepoint ASL would be preferred and the increase in postprocessing complexity can be accommodated.

2 | RECOMMENDATIONS

In this section, we outline the recommendations for multi-timepoint ASL methodology. We build on the 2015 consensus recommendations²⁰ and highlight areas of difference due to the specific considerations when using multi-timepoint ASL. Note: These recommendations have been made for a field strength of 3T and may be sub-optimal at other field strengths. Table 1 provides a concise summary of key acquisition and postprocessing recommendations.

2.1 | ASL labeling approaches

Due to its greater SNR, inherent control of the LD, compatibility with modern hardware, and wide-availability, PCASL⁵⁰ is also recommended for multi-timepoint ASL.

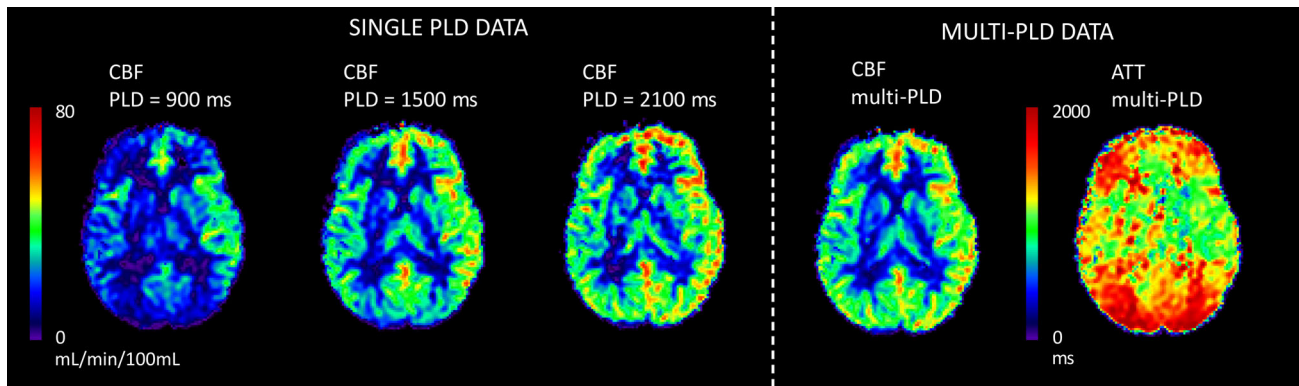


FIGURE 1 Demonstrating the relative insensitivity to ATT of multi-timepoint PCASL data. The single-PLD data show CBF underestimation in regions where the PLD is shorter than the ATT. When a sufficiently long PLD is used, the CBF estimated from single-PLD scans is relatively insensitive to ATT. However, by jointly fitting data at multiple PLDs to a kinetic signal model, ATT-insensitive CBF and ATT can be directly measured.

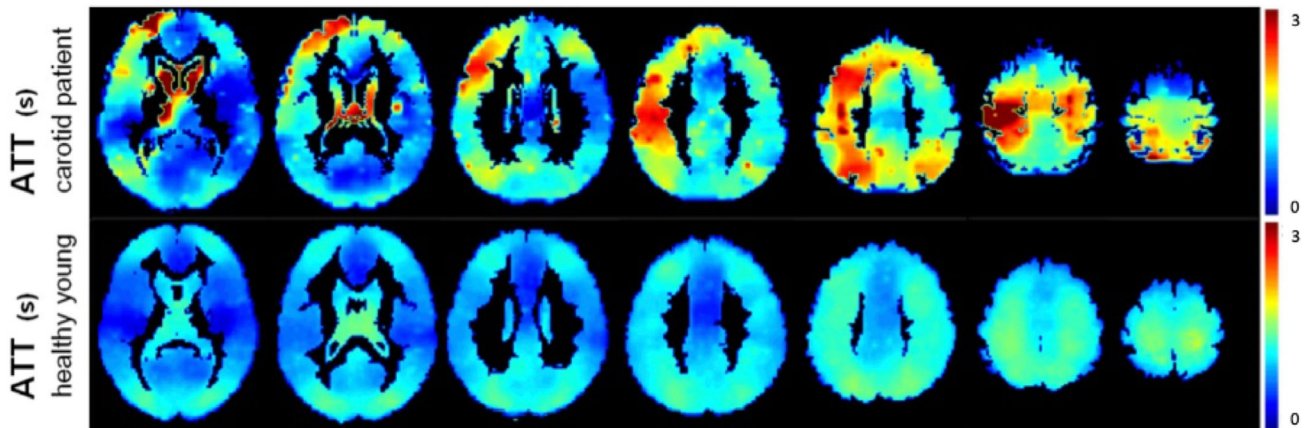


FIGURE 2 Demonstrating changes in ATT with disease. The top row shows ATT maps at various slices for a patient with carotid artery occlusion, while the bottom row shows group average ATT maps from nine healthy young subjects. The data were corrected for PVEs³¹ and represents estimates of pure GM ATT. Note the left–right symmetry and overall lower ATT in the healthy young subjects compared to the patient. ATTs in the ipsilateral hemisphere were on average ~1 s longer for the patient. Figure reproduced from Ref 32 with permission.

Given our recommendation for using PCASL as the labeling technique, many of the following recommendations refer specifically to this technique.

Although pulsed ASL (PASL)^{51–54} can also be used for multi-timepoint measurements, it has lower SNR. However, when ATT is the primary measurement of interest, rather than CBF, PASL could be considered unless very long ATTs are expected. This is because it is possible to sample more of the label inflow with PASL than with PCASL without reducing the LD. In cases when PASL is used, the QUIPSS II/Q2TIPS^{21,55} modification is recommended to control the LD and avoid the need for estimating it during postprocessing. A particular implementation of such methods, in combination with multiple Look-Locker-like readouts, is used in the QUASAR technique.⁵³

Velocity-selective ASL⁵⁶ is a highly promising alternative to multi-timepoint PCASL/PASL for measuring ATT-insensitive CBF, although in its traditional form cannot measure ATT. The negligible transit time in velocity-selective ASL⁵⁷ makes it a particularly robust choice for measuring CBF in cases of severely delayed blood arrival.⁵⁸ A review of velocity-selective ASL and associated recommendations can be found in Ref 22.

2.2 | Labeling: spatial placement

An important consideration for multi-timepoint measurements is the PCASL labeling plane location because this has a direct impact on the measured ATT.⁵⁹

Simple placement options, which only require a fast localizer scan, include placing the labeling plane 85 mm

TABLE 1 Major recommendations for quantitative cerebral perfusion MRI using multi-timepoint ASL.

Key multi-timepoint recommendations
Acquisition
1. Use of pseudo-continuous ASL (PCASL).
2. Protocol design: either sequential, time-encoded and hybrid methods (see Figure 3), depending upon availability and application.
3. Use of variable TRs, where the TR is minimized for each LD/PLD combination, for greater time efficiency.
4. Optimize the background suppression (BS) inversion timings for each TR.
5. Sequence looping: inner-loop is ASL condition (label/control conditions or time-encodings), followed by image segments, then LD/PLD adjustments, with averages in the outermost loop.
6. Scan duration: a protocol of minimum ~4 min for quantitative multi-timepoint ASL at 3T when reliable parameter estimates are required at an individual level.
Postprocessing
7. At minimum, estimate perfusion and ATT from multi-timepoint data using a kinetic signal model.
8. Use of an extended version of the single-PLD ASL quantification model from the 2015 consensus paper that incorporates the effects of variable ATT (Eqs. 2 and 3)
9. In general, model intravascular signals rather than suppress them.
10. When vessel suppression has not been used, include an extra intravascular component in the quantification model (Eq. 6).
11. Use of motion correction to further reduce the impacts of motion beyond what BS can achieve.

inferior to the anterior commissure-posterior commissure line in adults or just below the inferior border of the cerebellum, although placement between the second and third cervical vertebrae may be more robust across subjects.⁶⁰ Greater robustness to reduced labeling efficiency in one or more arteries due to tortuous blood flow can be achieved by using an angiographic survey to place the labeling plane. However, because labeling plane placement is particularly robust to angulation of the carotid arteries due to their fast blood flow velocities,⁶¹ any additional placement efforts should focus on robust positioning relative to the vertebral arteries. Care should also be taken to avoid placing the labeling plane near dental implants that can lead to large resonance offsets, reducing labeling efficiency.

Within a study, consistency of positioning, robustness within a given workflow, and avoidance of direct tissue saturation effects within the imaging region are key considerations for labeling plane location. It should be noted that positioning is fixed in many commercial implementations. In all cases, we recommend the positioning strategy be reported to allow others to reproduce the protocol.

2.3 | Protocol timings

Unlike single-PLD ASL, where multiple volumes are acquired with the same fixed LD and PLD, a multi-timepoint protocol acquires multiple label/control image pairs with a combination of different LDs and/or PLDs. Many methods for acquiring this dynamic data have

been developed and, while they can all be successfully utilized, each has advantages and disadvantages which we have summarized here. We recommend that one of the strategies illustrated in Figure 3 is used to achieve a range of LDs and/or PLDs, including sequential, time-encoded and hybrid methods, depending upon availability and application.

Although multi-timepoint ASL requires the acquisition of more than a single label/control pair, the scan time need not be longer than that of a single-PLD acquisition, where the minimum recommended scan time is ~2 min²⁰ due to necessary signal averaging. This is typically sufficient to acquire four to five different timepoints, depending on the type of readout used (e.g., single-shot EPI, multi-shot/segmented 3D methods), and although fewer averages can be acquired at each timepoint, the data are combined during the fitting process, thus achieving a similar level of signal averaging and noise suppression to single-PLD ASL but with the advantage of additional hemodynamic information.^{27,62}

2.3.1 | Sequential

The simplest approach to acquire multi-timepoint data is to perform a series of single-PLD scans with varying PLDs.^{3,23,24,63} However, we recommend that the PLDs are interleaved as much as possible so that the distribution of PLDs acquired at any given time closely matches the final targeted distribution. When each PLD has the

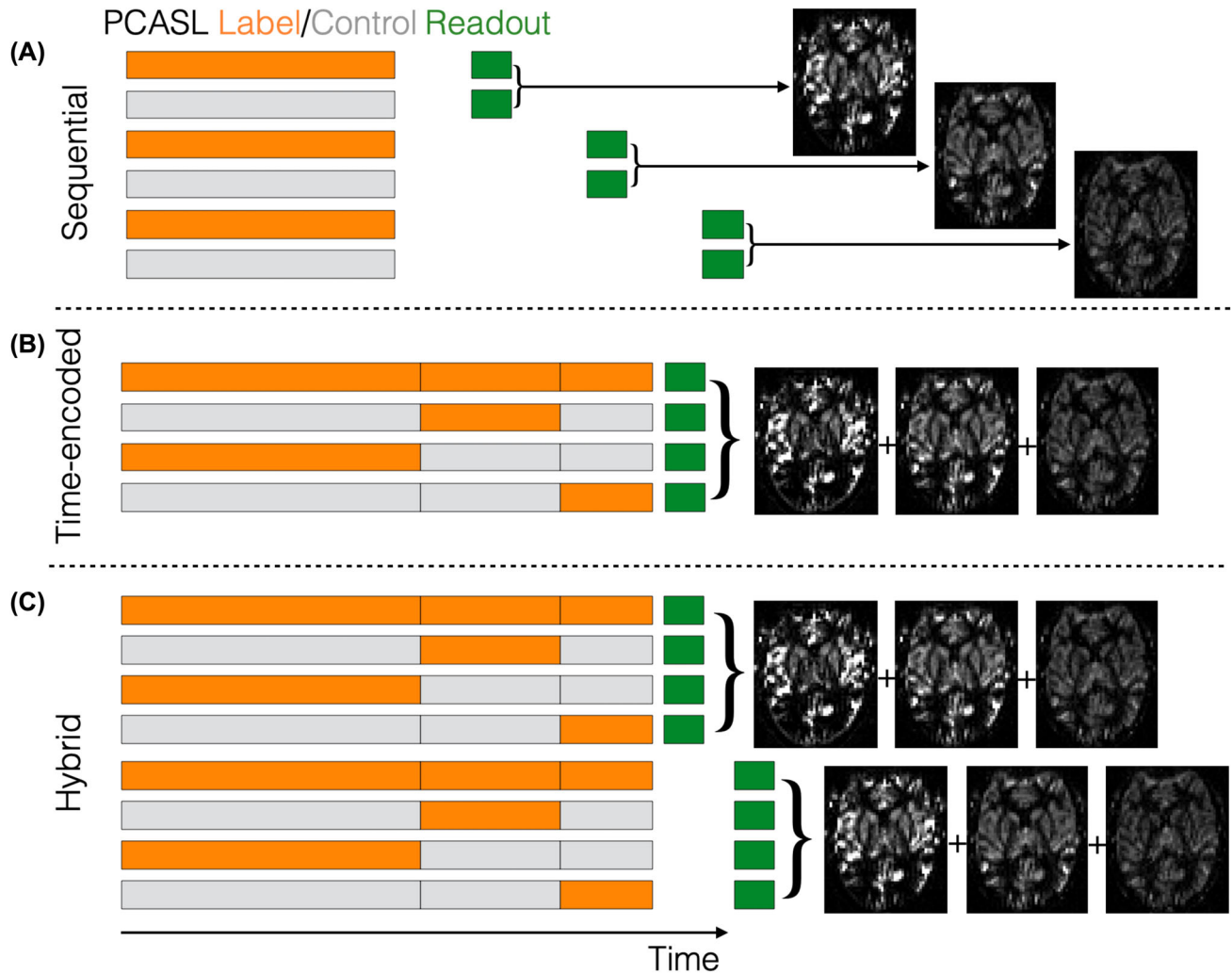


FIGURE 3 Illustrating the timing principles of the recommended multi-timepoint PCASL protocol types. The LDs are depicted as orange and gray boxes, representing label and control conditions, respectively. The PLD is the time between the end of the LD and the start of the image readout. Adapted from Ref 49 with permission.

same number of averages, this is simply achieved by the sequence looping over each PLD before acquiring the next average. This may reduce motion artifacts by minimizing the acquisition time between each PLD, but also distributes the PLDs throughout the scan, potentially reducing measurement bias from transitory physiological variation. The repeated acquisitions can then be averaged at the end of the scan for visualization. This approach is referred to as sequential multi-timepoint ASL.

Sequential PCASL (Figure 3A) is widely available and may be more robust to subject motion than time-encoded PCASL but, in general, it has lower CBF and ATT precision than hybrid protocols and lower ATT precision than time-encoded protocols (see below).²⁷ Although the LD is often kept constant, it can also be varied with the PLD when using PCASL to provide greater time efficiency^{57,64–66} and increased measurement precision.²⁷ Finally, to achieve greater time efficiency, we recommend

using variable minimum TRs, where the TR is minimized for each LD/PLD combination in the acquisition (i.e., the time between the end of the readout in one TR and the start of labeling in the next TR is fixed and minimal). When using variable minimum TRs, particular care should be taken to robustly saturate the imaging volume at the start or end of each TR.

2.3.2 | Time-encoding

Time-encoded PCASL^{25,26,67–68} (Figure 3B, sometimes referred to as “Hadamard-encoded PCASL”) was introduced as a time-efficient alternative to sequentially varying the LD and PLD. Rather than acquiring each image with a single combination of LD and PLD, the PCASL preparation is split into multiple sub-boluses. Each sub-bolus has an effective LD and PLD and the acquired

images contain a mixture of their signals. The label/control conditions for each sub-bolus are varied across multiple TRs using a linearly independent pattern. Subsequently, signals associated with each sub-bolus can be separated via simple addition and subtraction of the acquired images in a process called “decoding” (see Figure 4).

Hadamard encoding⁶⁹ is typically used to define the encoding pattern because of its optimal efficiency: only N images are required to decode $N-1$ timepoints and the measurement noise is reduced by a factor of $N/2$ compared to a matched sequential protocol.²⁵ However, because the labeling period is split into multiple sub-boluses, most of the sub-boluses have relatively short LDs (see Table 2), resulting in lower signal compared to the typically long LDs used in sequential acquisitions. This can decrease, and sometimes outweigh, the noise averaging benefits for CBF accuracy compared to sequential acquisitions, depending on the protocol timings (e.g., see the similar CBF errors for time-encoded and sequential protocols in Figure 5).^{27,70} Nevertheless, time-encoded preparations generally have superior ATT accuracy.^{27,70}

Two time-encoded protocols have, so far, proved particularly SNR-efficient for CBF measurement and are similar in that they seek to use longer LDs for sub-boluses which have longer PLDs. One is the “free-lunch” approach,^{67,68} where the first sub-bolus has a long LD and PLD,

similar to single-PLD PCASL,²⁰ but the PLD is filled with the remaining time-encoded sub-boluses. The other is the T_1 -compensated protocol,⁶⁷ where the LDs of each sub-bolus are chosen such that the total signal of each decoded perfusion-weighted image is equal, that is,

$$LD_i = T_{1b} \cdot \ln \left(1 + \left(1 - e^{-\frac{LD_1}{T_{1b}}} \right) \cdot e^{-\frac{t_i}{T_{1b}}} \right) \quad (1)$$

for $i = 2, \dots, N$, where N is the number of sub-boluses, LD_i is the i^{th} LD, t is the time from the end of first LD to the start of the i^{th} LD, with $t_2 = 0$ and $t_i = \sum_{n=2}^{i-1} LD_n$, and T_{1b} is the longitudinal relaxation time of blood. The minimum LD should generally be >50 ms to avoid signal loss due to bolus dispersion.⁶⁷

A possible downside of time-encoding is its higher sensitivity to image artifacts, especially those arising from motion, because more than two images must be combined to generate the individual difference images associated with each sub-bolus. Hence, unlike sequential acquisitions, it is not possible to individually remove corrupted label/control pairs. This increased motion sensitivity can be mitigated by using effective BS and Walsh-ordering of the Hadamard matrix.⁷¹ Despite this drawback, time-encoding has been successfully used in a range of clinical and research applications.^{25,72,73}

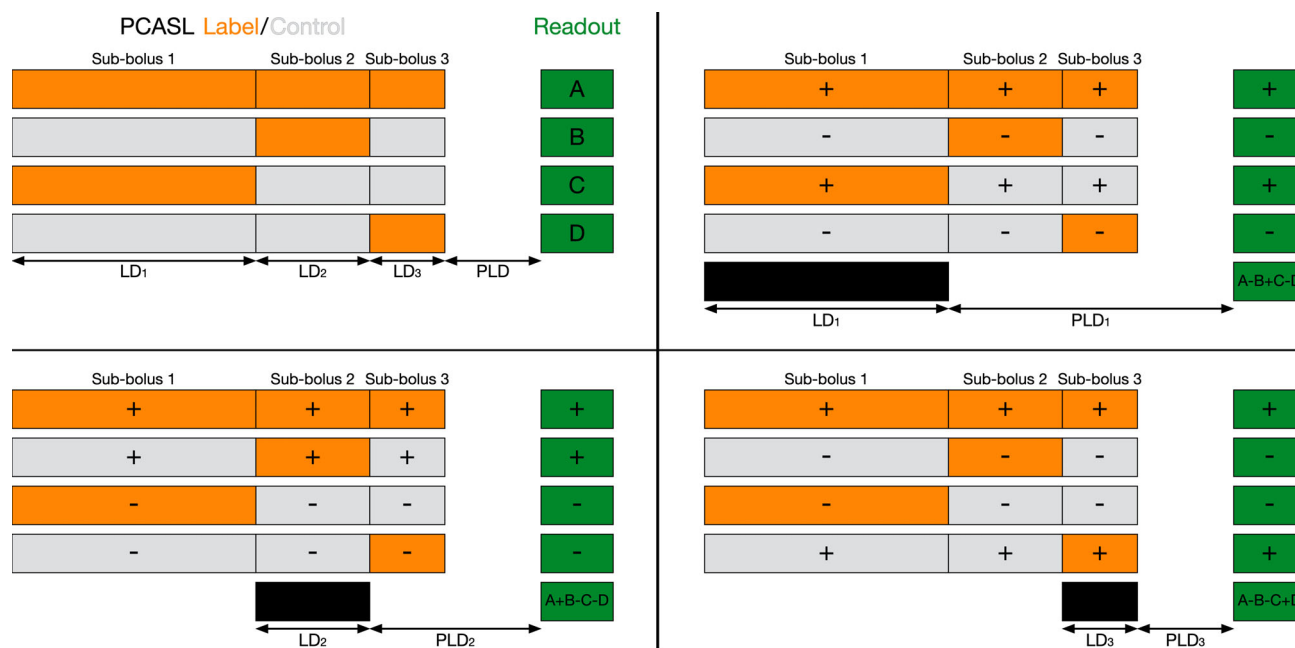


FIGURE 4 Demonstrating the time-encoded timing decoding process for a 4×3 Hadamard encoding pattern. Four encoded images (A, B, C, D, shown in green) are acquired from which three perfusion weighted images can be decoded, each with a different LD and effective PLD. The LDs are depicted as orange and gray boxes, representing label and control conditions, respectively. The process of decoding each of the three perfusion weighted images are shown top-right, bottom-left, and bottom-right. The equivalent LDs and PLDs of each decoded perfusion weighted image for a sequential multi-timepoint protocol are shown as black boxes.

TABLE 2 3T multi-timepoint PCASL protocol timings optimized for CBF and ATT using two ATT ranges: 0.5–1.8 s (a typical ATT range for young healthy subjects) and 0.5–2.5 s (an extended ATT range for more robust use in older and clinical subjects).

Protocol	LDs (ms)	PLDs (ms)	N_T	N_{Ave} / N_{Seg}	N_{Acq}	Scan duration (min:s)
ATT range 0.5–1.8 s						
Sequential Multi-PLD	2175	100, 100, 1275, 1800, 2100	5	8	80	5:00
Sequential Multi-LD/PLD	1925, 1825, 2300, 2300, 2300	175, 300, 1300, 1750, 2050	5	8	80	5:00
Time-encoded T_1 -compensated	1550, 775, 525, 400, 325, 275, 225	100	7	8	64	4:59
Hybrid T_1 -compensated	2250, 925, 575	175, 350, 600, 625	12	4	64	4:43
ATT range: 0.5–2.5 s						
Sequential Multi-PLD	2050	200, 775, 775, 775, 1800, 2275, 2475, 2675, 2800	9	4	72	5:00
Sequential Multi-LD/PLD	2300, 1850, 1825, 1800, 1150, 2300, 2300, 2300, 2300	200, 975, 1000, 1025, 1675, 2125, 2375, 2625, 2775	9	4	72	4:59
Time-encoded T_1 -compensated	2150, 900, 575, 425, 350, 275, 250, 200, 175, 175, 150	100	11	4	48	4:59
Hybrid T_1 -compensated	1800, 850, 550	150, 1025, 1350, 1400	12	4	64	5:00

Note: When LD/PLD combinations are repeated multiple times, it means these timings are effectively acquired with more averages. For the sequential multi-LD/PLD protocols, each LD is used with the corresponding PLD in the ordered list, i.e., LD₁ with PLD₁. For the hybrid protocols, the same three encoded LDs are used with each final PLD. Protocol optimization settings: maximum scan duration = 5 min, T_{1b} = 1.65 s, minimum PLD = 100 ms, minimum/maximum LD = 50/2300 ms, 500 ms of non-ASL time (readout, etc), minimum variable TR. The ATT probability was uniform across each ATT range and the ATT distribution was sampled every 10 ms. A linearly decreasing ATT probability extended 300 ms either side of the ATT range to avoid the measurement uncertainty increasing at the ATT distribution edges. Originally optimized for a 75 s scan time to allow time for four readout segments within a 5-min scan. Abbreviations: N_{Acq} = total number of acquisitions (one acquisition is one label/control/encoded image); N_{Ave} , number of averages; N_{Seg} = number of readout segments; N_T , number of timepoints.

2.3.3 | Time-encoded/sequential hybrid

A more flexible alternative to pure time-encoding is to sequentially repeat a time-encoded protocol with different final PLDs.²⁷ This hybrid protocol (Figure 3C) enables the use of longer LDs than pure time-encoding because a 4×3 Hadamard encoding can be used (smaller than the more typically used 8×7 or 12×11 encodings), while sufficient temporal information for accurate measurement is generated from both the time-decoding and multiple PLDs (the number of decoded timepoints being three times the number of final PLDs for a 4×3 encoding). This approach has been shown to provide more precise CBF measurements than other multi-timepoint protocols²⁷ and the use of a smaller time-encoding matrix reduces motion sensitivity. To further minimize motion sensitivity, the sequence

should ideally loop over the encodings, then PLDs, then averages, but a standard time-encoded scan can also simply be repeated with different PLDs.

2.3.4 | Look-Locker

Multiple timepoints can also be obtained using a Look-Locker readout,^{28,53,74} where multiple images are acquired with different PLDs after a single ASL preparation. This can be an attractive approach because the time taken to acquire all the PLDs can be reduced compared to other multi-timepoint protocols, making it more robust to subject motion and more suitable for measuring short time-scale perfusion changes. Look-Locker readouts can also be combined with time-encoded PCASL to generate very high temporal resolution data.⁷⁵

However, there are several limitations of using Look-Locker ASL. First, labeled blood within the imaging volume is attenuated by repeated readout excitations, so low excitation flip angles are necessary to preserve signal for later timepoints,^{76,77} which reduces SNR. Second, this attenuation must be accounted for during quantification, which is made difficult due to uncertainty in how much of the bolus was attenuated by each excitation.^{28,74,78} Third, background signal can typically only be suppressed at a single time point, so, as with multi-slice readouts, the effectiveness of BS is reduced (see below). Finally, brain coverage is limited by the time interval between two consecutive measurements (typically five to seven slices are compatible with a 250–300 ms temporal resolution),^{79,80} although simultaneous multi-slice (SMS) can be used to increase coverage.^{75,81,82} Due to its reduced SNR and the increased difficulty in its use, Look-Locker ASL is not recommended for routine use if one of the above alternatives is available.

2.3.5 | MR fingerprinting ASL

Multi-timepoint data can also be acquired using an MR fingerprinting approach.^{83–86} In ASL fingerprinting, a series of images is acquired with varied label/control PCASL preparations. Unlike other ASL protocols, the image volume is not saturated between acquisitions, so each image contains contributions from a number of previous label/control preparations. Although an almost zero PLD is typically used, a diverse range of temporal information is encoded by pseudo-randomly varying the LD and label/control order. MRF ASL is still considered to be an experimental method; further details can be found in.⁸⁷

2.3.6 | Optimal timings

The choice of LDs, PLDs, and number of timepoints acquired directly affects the precision and bias of the parameters estimated (typically CBF and ATT as a minimum). In the literature, protocol timings are often chosen empirically. However, timings which maximize measurement precision may also be chosen objectively using the Cramér-Rao lower bound (CRLB), a statistical expression that describes the lower bound of the estimated parameter variances.⁸⁸

The use of the CRLB for finding optimal multi-timepoint protocol timings has been widely demonstrated for CBF and ATT estimation,^{27,28,62,74,83,89–98} and we recommend that CRLB optimized protocol timings are

used for quantitative imaging, when possible, to maximize measurement precision and scan efficiency.

While measurement precision can typically be maximized with many single-average unique timepoints,⁶² it is often simpler to design an acquisition with a fixed number of unique timepoints and repeat this set as needed to achieve sufficient SNR. In practice four to seven unique timepoints is generally sufficient to estimate CBF and ATT and can be designed to offer superior precision to a single-PLD acquisition.²⁷

Timings, optimized for both CBF and ATT precision, for several classes of PCASL protocol at 3T, covering typical ranges of ATT (0.5–1.8 s and 0.5–2.5 s) and constrained to a 5-min scan duration, are provided in Table 2 with the simulated measurement errors for these protocols, and two single-PLD protocols for comparison, shown in Figure 5. These multi-timepoint protocol timings were generated using freely available open-source software (https://github.com/physimals/oxasl_optpcasl) which readers are encouraged to use if their scan requirements differ substantially from those provided, for example, different field strength (affecting T_{1b}) or incompatible readout segmentation. Note, improved multi-timepoint CBF accuracy can be achieved by optimizing the protocol timings for just CBF precision.⁶²

As can be seen in Figure 5, the hybrid protocols have the lowest multi-timepoint simulation CBF errors while having similar ATT errors to the time-encoded protocols. The sequential protocols have similar simulation CBF errors to the time-encoded protocols but generally have larger ATT errors. Compared to the single-PLD protocols, which do not provide estimates of ATT, the hybrid protocols achieve lower CBF errors for the majority of the ATT ranges (except for the largest ATTs, which are close in value to the single-PLD value). Although these simulations demonstrate that some multi-timepoint protocols can theoretically provide lower CBF errors than single-PLD ASL, it is currently unclear whether this benefit outweighs the increased postprocessing complexity in clinical settings, unless ATT maps are also required.

While it is possible to measure perfusion when ATTs are longer than 2.5 s, T_1 -relaxation of the label means that the measurements will have low precision within such short scan durations; longer scan durations or the use of velocity-selective ASL²² may be more appropriate in such cases. The use of longer LDs than those used here (max LD = 2.3 s) can improve CBF precision,²⁷ but long LDs can also increase the influence of tissue T_1 on the signal, potentially increasing measurement bias unless tissue T_1 is separately measured and included during perfusion quantification (see Section 2.7.4).

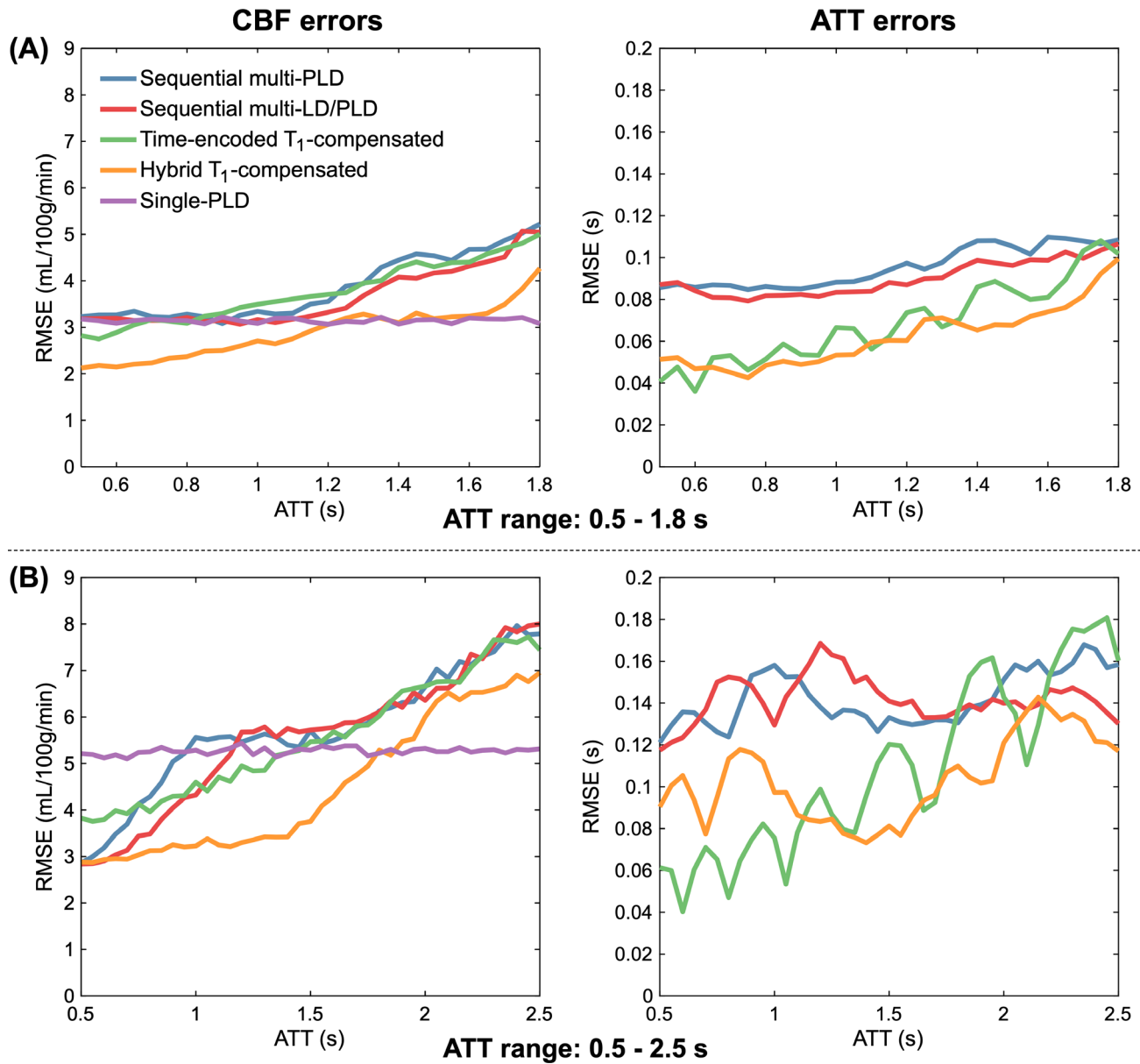


FIGURE 5 Monte Carlo simulation CBF and ATT quantification errors for the protocols shown in Table 2 and two single-PLD protocols. (A) The quantification errors for the short ATT range, 0.5–1.8 s (single-PLD: LD = 1800 ms, PLD = 1800 ms, $N_{Ave}/N_{Seq} = 37$, scan duration 5:03 min); (B) the quantification errors for the extended ATT range, 0.5–2.5 s (single-PLD: LD = 1800 ms, PLD = 2500 ms, $N_{Ave}/N_{Seq} = 31$, scan duration 4:58 min). The RMSE was used as a general measure of error because it is a combination of both measurement bias and SD.⁶² The data were simulated and fit using the PCASL signal model in Eq. (3) with $\alpha = 0.85$, $\alpha_{BS} = 1$, $M_{0a} = 1$, CBF = 50 mL/100 g/min, $T_{1b} = 1.65$ s. White Gaussian noise was added to 2000 copies of each simulated control/label/encoded “image” before subtraction/decoding. The noise SD was $M_{0a} \cdot 1.4 \cdot 10^{-3}$, equivalent to a noise SD of 38% of the ASL signal or an SNR of 2.63 for a single control-label difference image with LD = PLD = 1.8 s, $T_{1b} = 1.65$ s, and ATT < 1.8 s. Model fitting used a non-linear least squares approach similar to that described in Ref 62.

2.4 | Background suppression

BS is used to improve the SNR of ASL perfusion scans.^{99–103} Improvements in temporal SNR of 2–3x can be expected,^{103–105} although the effectiveness of BS with 2D multi-slice and Look-Locker acquisitions is reduced because background signal is typically only optimal for the first PLD.

In multi-timepoint acquisitions, the time between the presaturation and readout often varies with each LD/PLD pair for time-efficiency, for example, when using minimum variable TR. Because the use of identical inversion BS timings for all acquired timepoints results in sub-optimal BS, we recommend that the BS inversion timings are optimized for each TR in a multi-timepoint ASL sequence. These timings are ideally

calculated on-the-fly so that users can flexibly change scan timings.^{100,101}

With PCASL, the BS inversion pulses are often placed during the PLD. However, this is often sub-optimal, particularly for long LD/short PLD combinations, for example, time-encoding. We recommend BS inversion pulses are interleaved with PCASL labeling when necessary to improve BS performance.^{25,27,30,101,106,107} When this occurs, the following adjustments are required: (1) the label/control condition for the remaining labeling period should be switched after each interleaved pulse is applied; (2) the BS inversion pulses should be slab-selective with the inferior edge parallel to and coincident with the PCASL labeling plane to invert already labeled/controlled blood while avoiding perturbing upstream arterial spins. For simplicity, the perfusion signal can be scaled by the net inversion efficiency of the BS inversion pulses in the same way as when they are not interleaved.¹⁰⁸

2.5 | Vessel suppression

At short PLDs, some labeled blood is likely to remain in the arteries, even among young healthy participants. Intravascular ASL signal can lead to local overestimation of perfusion and underestimation of ATT.^{30,109} For accurate quantification of perfusion, intravascular ASL signal should be either modeled or suppressed. In general, we recommend modeling intravascular signals rather than suppressing them (see Section 2.7.1), because they can contain clinically valuable information which vessel suppression can remove¹¹⁰ and vessel suppression typically reduces SNR due to T_2 or T_2^* decay. However, whether including additional intravascular model parameters leads to more or less perfusion measurement uncertainty than using vessel suppression is an unanswered question that requires further research. It is important to note that vessel suppression is commonly applied along a single flow-direction, leading to imperfect suppression.⁴⁵ Nonetheless, there may be cases when vessel suppression is preferred, such as in tumor imaging,¹¹¹ making it a valuable option for multi-timepoint ASL.

While the additional ASL signal attenuation from vessel suppression can be modeled, it is simpler and more robust to apply the same vessel suppression during acquisition of the calibration image, thus canceling out this effect after division by the reference image.³⁰

2.6 | Readout approaches

Segmented 3D readouts, such as 3D GRASE^{100,112,113} and 3D RARE stack-of-spirals,^{103,105} along with judicious use

of parallel imaging are recommended for ASL, when available, due to their compatibility with BS, identical PLD across slices, and high SNR.²⁰ With multi-timepoint ASL, the level of readout segmentation possible may be reduced for short scan durations due to the competing use of scan time for acquiring segments and temporal information. A rule of thumb is to only reduce the number of segments if the readout duration can be kept to <300 ms to avoid high levels of through-plane blurring,²⁰ but this will depend on the effective spatial resolution required.

Extending from the 2015 consensus paper, we recommend that the sequence first loops over the ASL condition (label/control conditions or time-encodings), followed by image segments to achieve the most accurate label/control subtractions.²⁰ This should then be followed by looping over LD/PLD adjustments, with averages in the outermost loop.

In some applications, including those where subject motion might be an issue, the use of single-shot 3D acquisitions may be desirable. Recent work has shown that single-shot readout durations can be reduced using in-plane partial Fourier combined with acceleration in the slice direction,¹¹⁴ acceleration along both phase encoding directions¹¹⁵ or employing 3D acceleration.¹¹⁶ Compressed sensing can also be used to exploit the temporal signal redundancy in multi-timepoint ASL by varying the undersampling pattern across timepoints, enabling increased acceleration factors.⁶⁶

2D single-shot readouts (e.g., EPI and spiral) are an adequate alternative when an optimized 3D readout is not available, although BS effectiveness is reduced and the PLD varies across slices, leading to slice-dependent CBF and ATT accuracy.⁶² SMS can increase the number of slices to achieve whole brain coverage,^{117,118} improve BS¹¹⁹ and reduce PLD differences across slices. However, the performance of postprocessing motion correction strategies can be compromised.¹²⁰

2.7 | Postprocessing methods

Whilst it is important for quality assurance to examine the ASL difference (control-label) images, we recommend that multi-timepoint ASL is processed using a quantification model to arrive at estimates of perfusion and ATT as a minimum. A major benefit of multi-timepoint ASL is being able to account for the effect of variable ATT on quantitative perfusion values and visualize the pattern of ATT itself. Since the tracer kinetics of the ASL label results in a signal model that is non-linear in ATT, it is not possible to use a single formula to compute perfusion, as was provided in the 2015 consensus paper. Instead, it is necessary to perform some form of algorithmic analysis. Although

this is more complex to implement, various existing algorithms and software tools are now readily available for this task (see: OSIP (Open Science Initiative for Perfusion Imaging) pipeline inventory).¹²¹

2.7.1 | Quantification model

The General Kinetic Model (GKM) is the most universal and widely used signal model for ASL. It was outlined in detail by Buxton et al.²⁹ following principles used in the early ASL publications^{52,122–124} and based on indicator-dilution theory.¹²⁵ By describing the delivery of labeled blood water to a voxel via an “arterial input function” and the subsequent behavior of that labeled blood water after arrival, via the “residue function,” the GKM provides a flexible way to incorporate a range of effects on the ASL signal.

In the 2015 consensus paper, several assumptions were made to derive a simplified model for perfusion quantification from single-PLD ASL based on the GKM. This was chosen as it can be used robustly in a wide range of circumstances without the need for more than a few key parameters to be set. We recommend that, in general, an extended version of this model is used for multi-timepoint data that incorporates the effects of variable ATT, but otherwise retains the other assumptions. This can be described by the following equations for PCASL and PASL:

PCASL:

$$\begin{aligned}
 &= 0 && 0 < LD + PLD < ATT \\
 SI_{control} - SI_{label} &= \frac{2 \cdot \alpha \cdot \alpha_{BS} \cdot T_{1b} \cdot M_{0a} \cdot CBF \cdot e^{-\frac{ATT}{T_{1b}}} \cdot \left(1 - e^{-\frac{LD+PLD-ATT}{T_{1b}}}\right)}{6000} && ATT < LD + PLD < ATT + LD \\
 &= \frac{2 \cdot \alpha \cdot \alpha_{BS} \cdot T_{1b} \cdot M_{0a} \cdot CBF \cdot e^{-\frac{PLD}{T_{1b}}} \cdot \left(1 - e^{-\frac{LD}{T_{1b}}}\right)}{6000} && ATT < PLD
 \end{aligned} \quad (2)$$

QUIPSS II/Q2TIPS PASL:

$$\begin{aligned}
 &= 0 && 0 < TI < ATT \\
 SI_{control} - SI_{label} &= \frac{2 \cdot \alpha \cdot \alpha_{BS} \cdot M_{0a} \cdot CBF \cdot e^{-\frac{TI}{T_{1b}}} \cdot (TI - ATT)}{6000} && ATT < TI < ATT + TI_1 \\
 &= \frac{2 \cdot \alpha \cdot \alpha_{BS} \cdot M_{0a} \cdot CBF \cdot e^{-\frac{TI}{T_{1b}}} \cdot TI_1}{6000} && ATT + TI_1 < TI
 \end{aligned} \quad (3)$$

where $SI_{control}$ and SI_{label} are respectively the signal intensities in a single pair of control/label images acquired with the same LD and PLD, α is the labeling efficiency, α_{BS} is the total BS inversion efficiency, T_{1b} is the longitudinal relaxation time of arterial blood in seconds, and M_{0a} is the equilibrium magnetization of arterial blood, calculated as $M_{0a} = SI_{PD}/\lambda$,^{126–128} where SI_{PD} is a proton density weighted image and λ is the tissue/blood partition coefficient (see Ref 128 for a detailed discussion of M_{0a} calibration approaches). The factor of 6000 converts the units for CBF from mL/g/s to mL/100 g/min. Note that for 2D multi-slice imaging, the PLD value should be adjusted for each slice to account for the time delay between slice acquisitions.

The major assumptions of this model are consistent with the recommended single-PLD formula, that is, (1) there is no outflow of labeled blood water and (2) the relaxation of labeled spins is governed by blood T_1 (or equivalently that blood T_1 and tissue T_1 are equal).²⁰ The second assumption may introduce appreciable errors where differences in T_1 between blood and tissue are large (e.g., in white matter [WM] and tumors) or when measurement times (LD + PLD) are long.¹²⁹ More complex models and separate measurements may be used to mitigate this, as discussed below.

When vessel suppression has not been used, we recommend that an extra intravascular component is included in the quantification model. The models in equations Eqs. (2) and (3) assume that all labeled blood water has arrived

in the capillary bed at the PLD, that is, it is a result of perfusive delivery to the tissue. Signal contributions arise from labeled blood water that remains in arterial vessels at the time of imaging: the so called “intravascular signal.” For the purposes of CBF quantification, this signal is regarded as artifactual, giving rise to overestimation of perfusion in voxels displaying intravascular contamination as the labeled blood water in the vessels is destined for delivery to tissue in other voxels via downstream capillary vessels. Since this signal is typically associated with larger arterial vessels with high flow speed compared to the rate of water exchange across the vessel walls, we recommend that this macrovascular component is modeled with the same form as the arterial input function.⁴⁵ Using similar assumptions as above, this gives rise to the equation:

PCASL:

$$\begin{array}{l} 0 \\ \Delta M_{art} = 2 \cdot \alpha \cdot \alpha_{BS} \cdot M_{0b} \cdot aBV \cdot e^{-\frac{aBAT}{T_{1b}}} \\ 0 \end{array} \quad \begin{array}{l} 0 < LD + PLD < aBAT \\ aBAT < LD + PLD < aBAT + LD \\ aBAT < PLD \end{array} \quad (4)$$

QUIPSS II/Q2TIPS PASL:

$$\begin{array}{l} 0 \\ \Delta M_{art} = 2 \cdot \alpha \cdot \alpha_{BS} \cdot M_{0b} \cdot aBV \cdot e^{-\frac{TI}{T_{1b}}} \\ 0 \end{array} \quad \begin{array}{l} 0 < TI < aBAT \\ aBAT < TI < aBAT + TI_1 \\ aBAT + TI_1 < TI \end{array} \quad (5)$$

where ΔM_{art} is the macrovascular difference signal, aBV is the arterial blood volume, the fraction of the voxel occupied by the arterial vessel, $aBAT$ is the arterial bolus arrival time, describing the first arrival of the labeled blood water in the voxel within the arterial vessel, and the other parameters are as defined previously. Notably, for $PLD > aBAT$ (PCASL) or $TI > aBAT$ (PASL) no macrovascular signal is present, that is, this defines the conditions under which a vascular artifact would not be seen in the data.

The macrovascular signal contribution occurs in addition to the “tissue” component in equations Eqs. (2) and (3); hence, it is not dependent directly upon perfusion within that voxel. When including the macrovascular component, we can represent the right-hand side of Eqs. (2) and (3) as ΔM_{tiss} (i.e., the tissue perfusion signal component), and we have the full quantification model as

$$SI_{control} - SI_{label} = \Delta M_{tiss} + \Delta M_{art}. \quad (6)$$

2.7.2 | Model fitting

For multi-timepoint ASL, data at different timepoints need to be combined and multiple parameters estimated. Various methods have been used to estimate kinetic model parameters in the literature, but the majority can be viewed as some form of nonlinear regression. There are examples of semi-parametric approaches being used to estimate a surrogate of the ATT from features of the multi-timepoint time course and using this ATT surrogate in the calculation of CBF.^{30,53,130} Alternatively, the GKM may be fit directly to the data for CBF and ATT using a nonlinear model fitting algorithm such as non-linear least squares²⁹ or Bayesian inference.¹³¹ The advantage of a full model-based fitting is the ability to flexibly extend the model and fit more parameters, for example, the

macrovascular component, where the data allows. There are few studies directly comparing different ASL analysis algorithms,^{39,132} although the Open Science Initiative for Perfusion Imaging has developed inventories of ASL software tools¹²¹ and challenges¹³³ to make systematic comparisons (www.osipi.org). There is currently no strong evidence to favor one algorithm over another in terms of accuracy, although features, for example, ability to model effects such as macrovascular contamination, spatial regularization, or uncertainty estimation might favor particular algorithms in specific cases.

Kinetic model analysis has been combined with the image reconstruction process to enable greater levels of acquisition acceleration by utilizing additional temporal model based sparsity.⁶⁶ In contrast to non-linear regression algorithms, MRF ASL has tended to employ dictionary algorithms (based on those used in the early MR fingerprinting literature).^{85,86} These are still based on a kinetic model description of the signal, but precompute various examples of the timecourse corresponding to the acquisition scheme used and find the closest match to the

data. These algorithms can offer fast processing and robust performance, especially when a more complex model is adopted, but can suffer from limitations due to the size of the precomputed dictionary and only being able to select from a discretized set of the parameter space. There are a growing number of examples of machine and deep learning analyses for MRI data, including ASL.^{83,134–136} For the most part these currently seek to learn either an existing kinetic model-based analysis or the relationship to another perfusion imaging measure. Such methods can offer fast analysis and robust solutions, but currently need to be trained for a specific acquisition protocol and do not generalize readily.

2.7.3 | Variation in blood T₁

Blood T₁ has a global scaling effect on the estimated perfusion and its value can be fixed according to literature values, for example, 1650 ms for 3T.¹³⁷ Experimental measurement of subject-specific blood T₁, either directly^{138–141} or using non-imaging parameters with a physiological model,^{137,142–144} can also be considered when blood T₁ deviates significantly from the normal range, such as in anemia¹⁴⁵ or gas challenges.¹⁴⁶ The value of obtaining per subject measures of blood T₁ will depend on the application, but there is some evidence that the reduction in perfusion bias from spending some of the available scan time measuring blood T₁ might outweigh the loss in precision for the ASL scan in terms of overall accuracy.¹⁴⁷

2.7.4 | Variation in tissue T₁

More complex models can mitigate the assumption that the relaxation of the labeled spins is entirely governed by blood T₁, accounting for the time the labeled blood water spends in the tissue. This is particularly important for non-cortical brain regions with shorter T₁ values such as WM, deep gray matter (GM) structures with high iron content such as the pallidum and putamen, and in tumors or other pathology where T₁ may be shortened.¹⁴⁸ In these situations, the single-compartment model of Buxton et al.²⁹ can be used with independent values for blood and tissue T₁, which can either be set using tissue specific literature values^{149,150} or measured using a separate scan. In cases where the tissue T₁ does not deviate greatly from typical values, it is unclear if the reduced perfusion bias from separately measuring tissue T₁ outweighs the loss in perfusion precision due to spending less of the available scan time on the ASL acquisition.

Although the tissue T₁ can be estimated from the ASL data itself during the quantification process (i.e.

simultaneously with CBF and ATT),⁶³ this decreases the precision and repeatability of the perfusion measurements, outweighing the benefits of reduced measurement bias for typical spatial resolutions and scan times.⁸⁹ Some ASL techniques,⁶⁵ including fingerprinting,^{84–86,134,136} use a saturation-recovery approach to provide another source of tissue T₁ information in the ASL data that is not coupled to the perfusion signal; however, this generally precludes the use of efficient BS.

Use of the model with separate blood and tissue T₁ introduces an additional assumption that labeled blood water exchanges instantaneously with tissue water as soon as it enters the tissue voxel (i.e., when LD + PLD > ATT). In practice, labeled spins will remain in the blood compartment for some time prior to exchange. More complex two-compartment models incorporating exchange time or permeability of the vessel wall to water can mitigate this assumption.^{129,151} However, knowledge of water exchange is then needed which is challenging and time-consuming to measure accurately.^{152–154}

2.7.5 | Bolus dispersion

In the standard ASL kinetic model, labeled blood moves downstream inside arteries under the assumption of a uniform velocity profile (plug flow). In reality, the bolus of labeled blood water may be subject to intravascular dispersion. Dispersion affects the temporal features of the intravascular ASL signal and consequently the estimated perfusion value through changes in the form of the arterial input function. In a single-PLD ASL experiment, it is not possible to reconcile these issues and, therefore, dispersion contributes to errors in perfusion estimation. Characterizing ASL dispersion itself may be of interest since the process relates to cardiovascular physiology. Pathological changes to the composition of arteries can increase arterial stiffness, altering the degree of ASL bolus dispersion.⁴⁷ Similarly, narrowing of the arterial lumen can alter the fluid mechanics inside the conduit ASL vessel.¹⁵⁵ However, few studies have investigated ASL dispersion in relation to the underlying physiological drivers.

More advanced models have been used to characterize dispersion, such as modeling dispersion using a vascular transport kernel^{47,153–157} or using typical intravascular flow velocity characteristics to describe the expected form of the arterial input.¹⁵⁸ Multi-timepoint measurements offer the possibility to detect variation in the signal due to dispersion and attempt to correct for it by inclusion of further dispersion parameters in the model fitting, potentially yielding further hemodynamic information in the process. The effects of dispersion are most noticeable on signal from arterial vessels and this has been used to characterize

dispersion in ASL using angiographic readouts.^{47,159,160} The effects of dispersion on perfusion estimates can be substantial,^{160–162} but can be hard to detect in the signal time course because dispersion effects can appear similar to variations in other model parameters. Consequently, fitting dispersion parameters accurately from ASL tissue signal is challenging unless high SNR and high temporal resolution data is available.¹⁶⁰

The most widely used model of dispersion thus far is the gamma vascular transport kernel,⁴⁷ which can be convolved with the above models. This provides a good fit to ASL data and is relatively mathematically simple, adding only two additional model parameters. To avoid the risk of overfitting when implemented in a model fitting algorithm, the dispersion parameters should be constrained to a realistic range, e.g., using a Bayesian prior, or fixed to literature values; for example, Ref 47 found values for the gamma vascular transport function of $s \sim 0.5$ and $p \sim 0.1$ in major arteries. Where a macrovascular component is present and included in the model, this may also be used to simultaneously estimate appropriate dispersion parameters for the dataset.

2.7.6 | Partial volume effects

Differences in perfusion demands between tissues, combined with the low spatial resolution of ASL images relative to anatomical tissue variation, leads to a partial volume effect (PVE): the voxelwise measured CBF is a tissue-weighted average measure.⁴⁶ Correcting for PVE is especially relevant in studies of aging and dementia because PVE is exacerbated by atrophy. Algorithms that correct PVE (PVEc) typically use PV information derived from a high-resolution anatomical scan.^{31,163} Given that this scan is already routinely acquired in imaging studies, we encourage PVEc to be performed as an additional analysis, especially for clinical studies and studies where structural and hemodynamic changes may co-occur.

Since each tissue compartment in the brain has different perfusion kinetics (WM typically has longer ATTs than GM), multi-timepoint ASL is particularly suitable for PVEc since it provides extra information for a PVEc algorithm to separate different tissue contributions.¹⁶³ PVEc with multi-timepoint ASL not only provides separate estimates of GM and WM perfusion but also ATT for both tissue components.

2.7.7 | Motion correction

Subtraction of label/control images is an essential step in ASL postprocessing¹⁶⁴ but makes ASL especially sensitive

to motion. Subject motion should, therefore, be minimized as much as possible, which is typically achieved with foam pads. While BS reduces the impacts of motion, in general, we recommend the use of motion correction as another important strategy. This can take the form of prospective motion correction,^{165,166} motion correction during image reconstruction,^{167–170} or image-based registration during postprocessing. Motion-correction of the unsubtracted image series using rigid-body transformations during postprocessing is most commonly used due to its wide availability. However, this type of motion correction can be challenging for data with efficient BS because there is little static tissue signal available.

It should be noted that, for multi-timepoint data, the effectiveness of BS can differ across the different PLDs, thereby leading to varying image intensities and contrasts of the unsubtracted static tissue across timepoints. This can lead to minor artifactual motion estimations across timepoints when using conventional image similarity-based motion correction algorithms,¹⁷¹ in a similar way to the varying image intensities of label and control images.¹⁷² Additional subtraction artifacts and challenges can also arise for motion correction when using simultaneous multi-slice readouts due to the abrupt changes in image intensities across slices.¹²⁰

2.8 | Multi-timepoint ASL in application

2.8.1 | Acquisition duration

As noted by the 2015 consensus, since the ASL perfusion signal is small, ASL relies on averaging to achieve sufficient SNR. For multi-timepoint ASL, as a minimum, a ~ 2 -min protocol including 5 different LD/PLD combinations may be sufficient to acquire quantitative parameter estimates. However, in general, a protocol of minimum ~ 4 min is recommended for quantitative multi-timepoint ASL at 3T with the recommended spatial resolution (3–4 mm in-plane, 4–8 mm through-plane)²⁰ when reliable parameter estimates are required at an individual level.

2.8.2 | Quality assurance

In addition to the quality assurance steps recommended in the 2015 consensus²⁰ (briefly summarized below for completeness), we also advise the following two steps for multi-timepoint ASL data:

1. Check the temporal dynamics. Scrolling through the different ASL timepoints is the most direct method

to identify transitory artifacts or unexpected dynamics (such as arteriovenous malformations [AVMs]), which may be less clear in the final CBF and ATT maps. This can be achieved by first averaging the repeated acquisitions at each timepoint after the control-label subtraction/decoding, then ordering them with increasing TI (LD + PLD). Inspecting the individual difference images can be a useful follow-up step to check the proportion of images at a given timepoint affected. Note, if both the LDs and PLDs are varied, it may be more complicated to manually interpret the signal dynamics.

2. Compare the quantified CBF and ATT maps. It is possible that regions that have both low CBF and very long ATTs (where the ATTs are equal to or greater than the longest PLDs used) may in fact be well perfused, but the longest PLDs used were too short to capture the arrival of the ASL label.

The summarized 2015 consensus quality assurance recommendations (see²⁰ for further details):

1. For PCASL scans, look for areas of low labeling efficiency.
2. Note the overall GM perfusion value.
3. Check for motion artifacts.
4. Look for intravascular artifacts.
5. Check the border-zone (watershed) regions for artifactually low perfusion which may be due to long ATTs (see new QA steps above).

2.8.3 | WM perfusion

Measurement of WM perfusion, and hence detection of WM perfusion abnormalities, is challenging due to low SNR caused by the lower blood flow and longer ATT of WM compared to GM.^{90,173–177} Partial voluming with GM may also mask WM perfusion signals in GM/WM border regions.¹⁷⁵ The earlier timepoints often used by multi-timepoint ASL strategies may not contribute to greater WM perfusion SNR when compared to the use of a single long PLD. Hence, where WM perfusion is specifically of interest, it may be beneficial to design the timepoints used to include longer ATT or specifically only for a range of ATT seen in WM. Acquisition at a lower spatial resolution,¹⁷⁷ or analysis which combines voxels into lower resolution elements, can increase SNR and PVEc can be used to separate WM signals.

3 | CLINICAL APPLICATIONS

In this section, we examine examples where multi-timepoint ASL may offer advantages over the existing consensus single-PLD approach.

3.1 | Cerebrovascular reactivity

CVR reflects the capacity of blood vessels to alter their caliber and thus modify CBF in response to a vasoactive stimulus, e.g., acetazolamide, CO₂, or breath-hold.^{178–180} This parameter has been shown to be impaired in pathologies where the cerebrovasculature is compromised, such as stroke,^{181,182} small vessel disease,^{183,184} glioma,^{185–187} and neurodegenerative diseases.^{188–191}

ASL has been increasingly used to map CVR due to its ability to provide non-invasive and quantitative measures of CBF changes, compared to indirect or invasive methods such as BOLD-fMRI or PET. However, the application of vasoactive stimuli can lead to changes in ATT (see Figure 6),^{192,193} potentially compromising CVR measurements when single-PLD ASL is used. Due to its robustness to changes in ATT, multi-timepoint ASL CVR measurements may, therefore, be more accurate than single-PLD ASL.^{11,194} However, the short duration of breath-holds can make the use of multi-timepoint ASL difficult for this type of stimulus.¹⁸⁰

3.2 | Steno-occlusive disease

In steno-occlusive diseases, significant transit delay can occur distal to the stenosis, resulting in elongated ATTs and associated transit artifacts when using single-PLD ASL. As the degree of stenosis may vary with disease severity and with underlying etiology, simply choosing a single longer PLD may not be the best approach, making multi-PLD ASL highly relevant for these patients. Multi-PLD ASL has been utilized in steno-occlusive disease patients in both research and clinical settings, primarily in moyamoya disease^{195,196} but also in intracranial atherosclerotic disease.¹⁹⁷ In one cohort of patients with moyamoya, CBF derived using multi-PLD ASL showed a larger effect size than CBF from single-PLD ASL when comparing pre- and post-revascularization data.¹⁹⁸ In the same study, the additional ATT information from multi-PLD ASL was shown to be correlated with dynamic susceptibility contrast-based time-to-maximum values.¹⁹⁸ These data show the promise of multi-PLD ASL to provide similar information without the need for contrast injection. Another study in moyamoya patients demonstrated that hemodynamic parameters derived from multi-PLD ASL exhibited better agreement with analogous measures derived using oxygen-15 positron emission tomography than single-PLD ASL in both diseased and healthy brain hemispheres.¹⁹⁹ Together, these results support the use of multi-PLD over single-PLD ASL in patients with arterial steno-occlusive diseases.

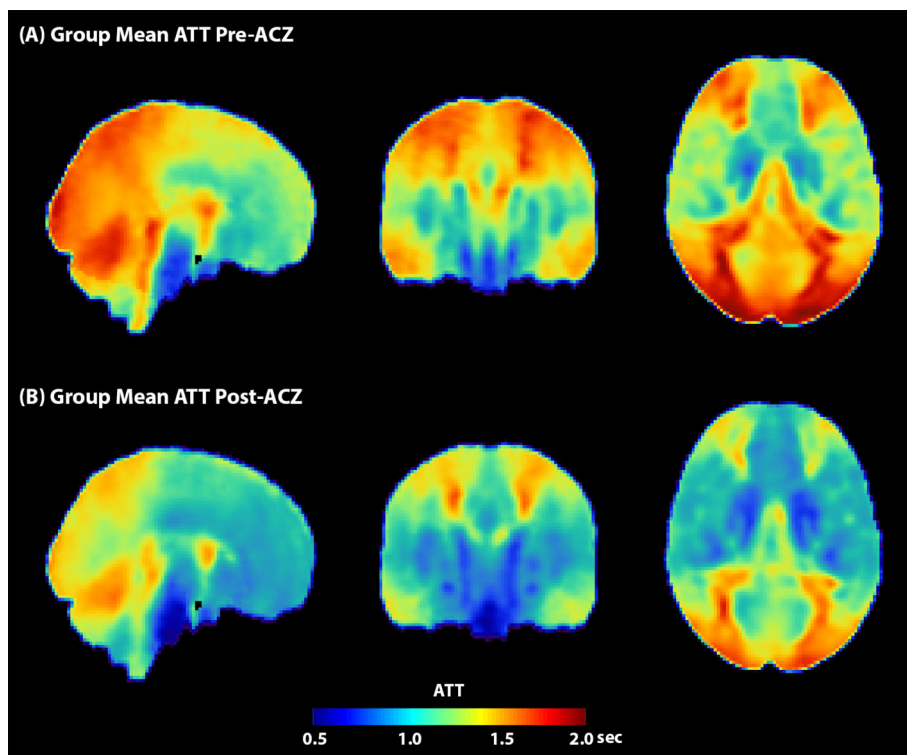


FIGURE 6 Brain-wide ATT changes before and after Acetazolamide administration. Note that, although both cases have similar watershed borders, the ATT is generally shorter after acetazolamide (B) than before (A). Figure reproduced from Ref 11 with permission.

3.3 | Arteriovenous malformations and fistulas

Cerebral AVMs and fistulas characteristically demonstrate abnormal arteriovenous connections (so-called shunts) that allow the ASL signal to bypass the capillary network, resulting in early venous arrival. This unique property of arteriovenous shunts (AVS) typically produces easily identifiable hyperintense venous ASL signal,^{122,200,201} although the degree of conspicuity is dependent on the LD and PLD.

While single-PLD ASL data, acquired using the 2015 consensus parameters, are often useful for assessing AVS, sensitivity may be degraded by several factors. First, single-PLD methods may miss or sub-optimally characterize lesions if shunt flow is too fast (resulting in complete venous clearance) or too slow (resulting in insufficient accumulation). Second, ambiguity will arise when it is unclear if the hyperintense ASL signal truly localizes to a vein versus a non-venous structure (e.g., a nearby artery or abnormal vascular tissue).

The qualitative use of multi-timepoint ASL addresses both issues. Short-PLD images improve assessment of high-flow shunts, whereas long-PLD images improve assessment of low-flow shunts. Since AVS are quite heterogeneous across the patient population, use of multi-timepoint ASL could effectively widen the operating range for ASL. Additionally, multi-timepoint ASL could allow a more comprehensive assessment of shunt flow by permitting a dynamic evaluation that would help spatially

localize arterial supply and venous drainage. This type of evaluation is particularly useful when following AVS over time to determine progression and/or response to therapy.

3.4 | Aging and neurodegenerative disease

ATTs have been shown to increase with age.^{130,202} Therefore, single-PLD ASL may not be well-suited for quantifying CBF in aging populations due to the large variability in the appropriate single-PLD. In these cases, multi-timepoint ASL may be appropriate to enable more accurate quantification of CBF in older adults and has recently been included in large consortium studies involving aging populations, including the Human Connectome Project-Aging,²⁰³ UK Biobank, and the Alzheimer's Disease Neuroimaging Initiative.²⁰⁴ Recent work has demonstrated that CBF measured using multi-timepoint ASL exhibited better agreement with CBF from ¹⁵O-PET and CT than single-PLD ASL in patients with pathologically long ATTs,^{6,195} and that it reduces the variability of CBF measurements in the frontal, parietal, and occipital brain regions in older adults.²⁰² Multi-timepoint ASL has also detected unique patterns in regional CBF in individuals who exhibited variable longitudinal changes in cognitive function.²⁰⁵

In addition to aiding in more accurate quantification of CBF, recent studies suggest that ATT can be used as a

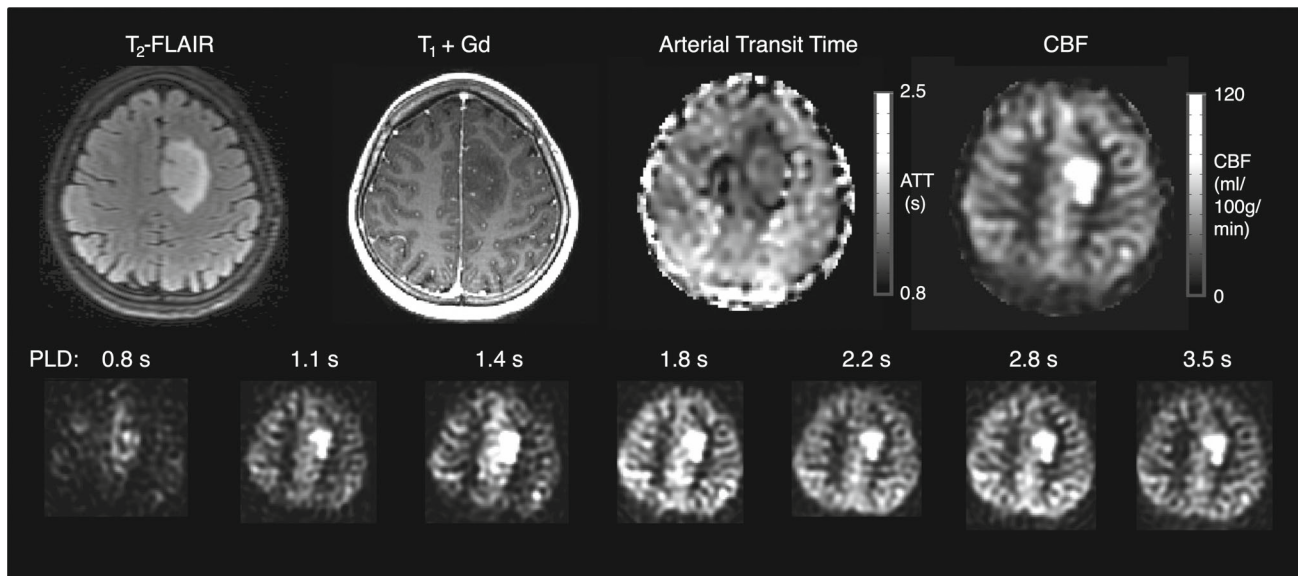


FIGURE 7 An example time-encoded multi-timepoint PCASL acquisition in a low-grade diffuse glioma (oligodendroglioma, WHO grade 2). Top row: The extent of the tumor can be seen in the T₂-FLAIR (hyperintense region). The T₁ + Gd shows no enhancement. The calculated PCASL CBF and ATT maps indicate an area of high perfusion with short arrival time within the tumor region, in part due to large intravascular signal contributions present in these data which were not modeled here. This is consistent with the finding that oligodendroglioma tend to be highly perfused and have high blood volume with irregular, although non-leaky, vasculature. Bottom row: perfusion-weighted images at each of the acquired PLDs.

cerebrovascular biomarker in aging and neurodegenerative diseases. One study showed that ATT was increased in several regions of interest (ROIs) in patients with Alzheimer's disease compared to healthy controls; and that this ATT increase was associated with cognitive performance.²⁰⁶ Parkinson's dementia²⁰⁷ and multiple sclerosis²⁰⁸ have also shown associations between ATT and cognitive decline. ATT proxies, such as FEAST-ATT²⁰⁹ and the spatial coefficient of variation (sCoV),²¹⁰ have also been used as potential biomarkers in neurodegenerative disease.

3.5 | Cancer

ASL is increasingly used clinically to aid the initial diagnosis of brain tumors and to monitor post-treatment to differentiate tumor recurrence from treatment effects.^{211,212} Although multi-timepoint ASL can provide greater CBF accuracy, brain tumor imaging may mostly benefit from its ability to characterize the arterial signal component and aBAT/ATT, due to the common irregular vasculature found with this disease (see Figure 7). For example, the vascular-weighted signal from early (<500 ms) PASL TIs have been shown to be superior to longer TIs in distinguishing between low- and high-grade astrocytoma and glioblastoma, improving pre-operative grading.²¹³ A further study demonstrated that multi-timepoint CBF

could distinguish between grade 2, 3, and 4 astrocytoma, whereas single-PLD CBF was only able to distinguish grade 2 and 4 tumors.²¹⁴ Another study found that, although multi-timepoint PASL with and without vascular crushing was not able to distinguish between different pediatric brain tumors (which DSC was able to), an improved picture was given of the tumor macro- and microvascular compartments.¹¹¹ The authors of the latter study also indicated that specifically in enhancing tumors, where DSC measurements are affected by leaky vessels, multi-timepoint ASL can likely improve knowledge on perfusion due to the ability to model ATT and intravascular signal. Future studies including multi-timepoint ASL in oncology are, therefore, warranted to further elucidate tumor hemodynamics.

4 | SUMMARY

ASL is now an established non-invasive technique for quantitatively imaging cerebral perfusion in both research and clinical settings. The recommendations provided in this paper aim to serve as a comprehensive guide for clinicians and researchers navigating the large array of options available when pursuing quantitative accuracy or the estimation of additional hemodynamic measures using multi-timepoint ASL. By employing a robust, yet relatively simple, multi-timepoint protocol, in conjunction with

widely available postprocessing techniques, more accurate and precise measurements of CBF can be achieved by accounting for variable ATTs and intravascular signal, as well as providing clinically valuable measurements of these physiological parameters. These guidelines do not intend to supersede the recommendations outlined in the 2015 consensus paper; rather, they offer specific guidance for utilizing multi-timepoint ASL methods that are already accessible to the research and clinical community through various vendor implementations and software toolboxes.

AFFILIATIONS

¹Wellcome Centre for Integrative Neuroimaging, FMRIB, Nuffield Department of Clinical Neurosciences, University of Oxford, Oxford, UK

²Center for Functional Magnetic Resonance Imaging, Department of Radiology, University of California San Diego, La Jolla, California USA

³Ghent Institute for Functional and Metabolic Imaging (GfMI), Ghent University, Ghent, Belgium

⁴Department of Neuroscience, University of Sussex, Brighton, UK

⁵Department of Biomedical Engineering, Rochester Institute of Technology, Rochester, New York USA

⁶Department of Computer Science, State University of New York at Binghamton, Binghamton, New York USA

⁷Department of Neurology, University of Pennsylvania, Philadelphia, Pennsylvania USA

⁸Department of Biomedical Engineering, University of California Davis, Davis, California USA

⁹Department of Neurology, University of California Davis, Davis, California USA

¹⁰Department of Radiology, Clínica Universidad de Navarra, Pamplona, Spain

¹¹IdiSNA, Instituto de Investigación Sanitaria de Navarra, Pamplona, Spain

¹²UCL Queen Square Institute of Neurology, University College London, London, UK

¹³Gold Standard Phantoms, Sheffield, UK

¹⁴Imaging Physics, Fraunhofer Institute for Digital Medicine MEVIS, Bremen, Germany

¹⁵Department of Physics and Electrical Engineering, University of Bremen, Bremen, Germany

¹⁶Department of Bioengineering, University of California Riverside, Riverside, California USA

¹⁷Department of Radiology, University of Michigan, Ann Arbor, Michigan USA

¹⁸Department of Radiology, University of Missouri, Columbia, Missouri USA

¹⁹Athinoula A. Martinos Center for Biomedical Imaging, Massachusetts General Hospital, Charlestown, Massachusetts USA

²⁰Department of Radiology, Harvard Medical School, Boston, Massachusetts USA

²¹The Russell H. Morgan Department of Radiology and Radiological Science, Johns Hopkins University School of Medicine, Baltimore, Maryland USA

²²Hurvitz Brain Sciences Program, Centre for Brain Resilience & Recovery, Sunnybrook Research Institute, Toronto, Ontario Canada

²³Department of Medical Biophysics, University of Toronto, Toronto, Ontario Canada

²⁴Computational Radiology & Artificial Intelligence unit, Oslo University Hospital, Oslo, Norway

²⁵Department of Radiology and Advanced Imaging Research Center, UT Southwestern Medical Center, Dallas, Texas USA

²⁶Department of Radiology and Nuclear Medicine, Amsterdam UMC location Vrije Universiteit Amsterdam, Amsterdam, The Netherlands

²⁷Amsterdam Neuroscience, Brain Imaging, Amsterdam, The Netherlands

²⁸School of Health Sciences, Faculty of Biology, Medicine and Health, University of Manchester, Manchester, UK

²⁹Geoffrey Jefferson Brain Research Centre, Manchester Academic Health Science Centre, Manchester, UK

³⁰Dent Neurologic Institute, Buffalo, New York USA

³¹University at Buffalo Neurosurgery, Buffalo, New York USA

³²Institute of Biomedical Engineering, Department of Engineering Science, University of Oxford, Oxford, UK

³³Department of Radiology & Nuclear Medicine, Erasmus MC, Rotterdam, The Netherlands

³⁴Medical Delta, Delft, The Netherlands

³⁵Erasmus MC Cancer Institute, Erasmus MC, Rotterdam, The Netherlands

³⁶Department of Brain Repair and Rehabilitation, UCL Queen Square Institute of Neurology, University College London, London, UK

³⁷C.J. Gorter MRI Center, Department of Radiology, Leiden University Medical Center, Leiden, The Netherlands

³⁸Laboratory of fMRI Technology (LOFT), Stevens Neuroimaging and Informatics Institute, University of Southern California, Los Angeles, California USA

³⁹Department of Radiology, Stanford University, Stanford, California USA

⁴⁰Department of Neuroimaging, Institute of Psychiatry, Psychology and Neuroscience, Kings College London, London, UK

⁴¹Maternal & Child Health Research Institute, Stanford University, Stanford, California USA

⁴²Sir Peter Mansfield Imaging Centre, School of Medicine, University of Nottingham, Nottingham, UK

ACKNOWLEDGMENTS

The work in this article has been endorsed by the ISMRM perfusion study section and by the ISMRM's board of trustees. Endorsement was obtained by a survey among the perfusion study group's members and by subsequent endorsement by the board of trustees.

J.G.W. and T.W.O. were supported by a Sir Henry Dale Fellowship jointly funded by the Wellcome Trust and the Royal Society (220204/Z/20/Z). J.G.W. acknowledges Linacre College (Oxford) for their support. The Wellcome Centre for Integrative Neuroimaging is supported by core funding from the Wellcome Trust (203139/Z/16/Z). A.P.F. was supported by the National Institute of Neurological

Disorders and Stroke (R00-NS-102884). J.G. was supported by US National Institutes of Health (R01EB033210). MRJ acknowledges funding from the US National Institutes of Health (K01-AG070318). A.J.M. acknowledges funding from the US National Institutes of Health/National Cancer Institute, U01 CA207091. M.J.Pv.O. acknowledges funding from the Dutch Research Foundation, VICI-project 016.160.351. J.P. was supported by the Engineering and Physical Sciences Research Council (EPSRC) grant EP/S021507/1. M.F.S. acknowledges funding from the Spanish Ministry of Science and Innovation (PI21/00578). D.L.T. was supported by the UCLH NIHR Biomedical Research Centre and the Wellcome Trust (Centre award 539208). G.Z. acknowledges funding from the US National Institutes of Health (R01-EB025220 & R01-NS123025).

Authors are listed in alphabetical order except for the first and last authors. For the purpose of open access, the authors have applied a CC BY public copyright license to any author-accepted manuscript version arising from this submission.

CONFLICT OF INTEREST STATEMENT

D.B. received research grant support from GE Healthcare. M.A.C. receives royalties from the commercial licensing of FSL and is an employee of, and holds equity in, Quantified Imaging Ltd. X.G. is a founder, shareholder and employee of Gold Standard Phantoms and a consultant at Bioxydyn. T.O. works as an ad hoc consultant for SBGNeuro Ltd. M.J.Pv.O. receives research support from Philips. M.S. received consultation fees from Bracco and a speaker fee from Istituto Internazionale Menarini (both paid to Erasmus MC). D.J.J.W. is a shareholder of Hura Imaging, INC. G.Z. receives grant support from GE Healthcare and Bayer Healthcare and has equity interest in Subtle Medical, Inc.

DATA AVAILABILITY STATEMENT

The MATLAB code used to perform the Monte Carlo simulations in Figure 5 are available at <https://doi.org/10.5281/zenodo.10642060>.

ENDNOTE

¹The timing parameters in ASL techniques, specifically (pseudo-)continuous ASL ((P)CASL) and pulsed ASL (PASL), have different terminologies. In (P)CASL, the LD and PLD are commonly used to describe the protocol timings. The LD represents the duration of the labeling period and, therefore, the duration of the labeled blood bolus. The PLD is the time between the end of labeling and the image readout. In PASL, the inversion time (TI) is used, which refers to the time between the labeling pulse and the image readout. TI includes both the labeled bolus duration (LD) and the PLD; specifically, $TI = LD + PLD$, where $LD = TI_1$ and $PLD = TI -$

TI_1 when QUIPSS II²¹ is used. To provide a more general terminology, we can refer to TI as the “inflow time”, with $TI = LD + PLD$, in both (P)CASL and PASL, as it represents the total time during which labeled blood can flow into the imaging region. It should be noted that the same definition of “inflow time” is also used in velocity selective ASL (VSASL), as described in the recent VSASL consensus paper.²²

ORCID

Joseph G. Woods  <https://orcid.org/0000-0002-0329-824X>

Eric Achten  <https://orcid.org/0000-0002-5148-4178>

Divya S. Bolar  <https://orcid.org/0000-0002-5968-2304>

Maria A. Fernández-Seara  <https://orcid.org/0000-0001-8536-6295>

Xavier Golay  <https://orcid.org/0000-0002-6447-4446>

Jia Guo  <https://orcid.org/0000-0003-3371-5857>

Luis Hernandez-Garcia  <https://orcid.org/0000-0003-3002-0304>

Mai-Lan Ho  <https://orcid.org/0000-0002-9455-1350>


Meher R. Juttukonda  <https://orcid.org/0000-0001-9064-3648>


Hanzhang Lu  <https://orcid.org/0000-0003-3871-1564>

Bradley J. MacIntosh  <https://orcid.org/0000-0001-7300-2355>

Ananth J. Madhuranthakam  <https://orcid.org/0000-0002-5524-7962>

Henk-Jan Mutsaerts  <https://orcid.org/0000-0003-0894-0307>

Thomas W. Okell  <https://orcid.org/0000-0001-8258-0659>

Laura M. Parkes  <https://orcid.org/0000-0001-6488-507X>

Nandor Pinter  <https://orcid.org/0000-0002-7714-143X>

Joana Pinto  <https://orcid.org/0000-0002-6863-1883>

Qin Qin  <https://orcid.org/0000-0002-6432-2944>

Marion Smits  <https://orcid.org/0000-0001-5563-2871>

Yuriko Suzuki  <https://orcid.org/0000-0002-4851-7872>

David L. Thomas  <https://orcid.org/0000-0003-1491-1641>

Matthias J. P. Van Osch  <https://orcid.org/0000-0001-7034-8959>

Danny J. J. Wang  <https://orcid.org/0000-0002-0840-7062>

Esther A. H. Warnert  <https://orcid.org/0000-0002-3196-1416>

Moss Zhao  <https://orcid.org/0000-0002-0210-7739>

Michael A. Chappell  <https://orcid.org/0000-0003-1802-4214>

TWITTER

Joseph G. Woods  [JosephGWoods](https://twitter.com/JosephGWoods)

REFERENCES

- Hara S, Tanaka Y, Ueda Y, et al. Noninvasive evaluation of CBF and perfusion delay of Moyamoya disease using arterial spin-labeling MRI with multiple Postlabeling delays: comparison with 15O-gas PET and DSC-MRI. *Am J Neuroradiol*. 2017;38:696-702. doi:10.3174/ajnr.A5068
- Martin SZ, Madai VI, von Samson-Himmelstjerna FC, et al. 3D GRASE pulsed arterial spin labeling at multiple inflow times in patients with long arterial transit times: comparison with dynamic susceptibility-weighted contrast-enhanced MRI at 3 tesla. *J Cereb Blood Flow Metab*. 2015;35:392-401. doi:10.1038/jcbfm.2014.200
- Wang DJJ, Alger JR, Qiao JX, et al. Multi-delay multi-parametric arterial spin-labeled perfusion MRI in acute ischemic stroke - comparison with dynamic susceptibility contrast enhanced perfusion imaging. *NeuroImage Clin*. 2013;3:1-7. doi:10.1016/j.nicl.2013.06.017
- Wong AM, Yan FX, Liu HL. Comparison of three-dimensional pseudo-continuous arterial spin labeling perfusion imaging with gradient-echo and spin-echo dynamic susceptibility contrast MRI. *J Magn Reson Imaging*. 2014;39:427-433. doi:10.1002/jmri.24178
- Dolui S, Vidorreta M, Wang Z, et al. Comparison of PASL, PCASL, and background-suppressed 3D PCASL in mild cognitive impairment. *Hum Brain Mapp*. 2017;38:5260-5273. doi:10.1002/hbm.23732
- Fan AP, Khalighi MM, Guo J, et al. Identifying hypoperfusion in Moyamoya disease with arterial spin labeling and an [¹⁵O]-water positron emission tomography/magnetic resonance imaging normative database. *Stroke*. 2019;50:373-380. doi:10.1161/STROKEAHA.118.023426
- Heijtel DFR, Mutsaerts HJMM, Bakker E, et al. Accuracy and precision of pseudo-continuous arterial spin labeling perfusion during baseline and hypercapnia: a head-to-head comparison with 15O H₂O positron emission tomography. *Neuroimage*. 2014;92:182-192. doi:10.1016/j.neuroimage.2014.02.011
- Tsujikawa T, Kimura H, Matsuda T, et al. Arterial transit time mapping obtained by pulsed continuous 3D ASL imaging with multiple post-label delay acquisitions: comparative study with PET-CBF in patients with chronic occlusive cerebrovascular disease. *PloS One*. 2016;11:e0156005. doi:10.1371/journal.pone.0156005
- Xu G, Rowley H, Wu G, et al. Reliability and precision of pseudo-continuous arterial spin labeling perfusion MRI on 3.0 T and comparison with 15 O-water PET in elderly subjects at risk for Alzheimer's disease. *NMR Biomed*. 2010;23:286-293. doi:10.1002/nbm.1462
- Zhang K, Herzog H, Mauler J, et al. Comparison of cerebral blood flow acquired by simultaneous [¹⁵O]water positron emission tomography and arterial spin labeling magnetic resonance imaging. *J Cereb Blood Flow Metab*. 2014;34:1373-1380. doi:10.1038/jcbfm.2014.92
- Zhao MY, Fan AP, Chen DYT, et al. Cerebrovascular reactivity measurements using simultaneous 15O-water PET and ASL MRI: impacts of arterial transit time, labeling efficiency, and hematocrit. *Neuroimage*. 2021;233:117955. doi:10.1016/j.neuroimage.2021.117955
- Mutsaerts HJMM, van Osch MJP, Zelaya FO, et al. Multi-vendor reliability of arterial spin labeling perfusion MRI using a near-identical sequence: implications for multi-center studies. *Neuroimage*. 2015;113:143-152. doi:10.1016/j.neuroimage.2015.03.043
- Petersen ET, Mouridsen K, Golay X. The QUASAR reproducibility study, part II: results from a multi-center arterial spin labeling test-retest study. *Neuroimage*. 2010;49:104-113. doi:10.1016/j.neuroimage.2009.07.068
- Detre JA, Rao H, Wang DJJ, Chen YF, Wang Z. Applications of arterial spin labeled MRI in the brain. *J Magn Reson Imaging*. 2012;35:1026-1037. doi:10.1002/jmri.23581
- Grade M, Hernandez Tamames JA, Pizzini FB, Achten E, Golay X, Smits M. A neuroradiologist's guide to arterial spin labeling MRI in clinical practice. *Neuroradiology*. 2015;57:1181-1202. doi:10.1007/s00234-015-1571-z
- Haller S, Zaharchuk G, Thomas DL, Lovblad KO, Barkhof F, Golay X. Arterial spin labeling perfusion of the brain: emerging clinical applications. *Radiology*. 2016;281:337-356. doi:10.1148/radiol.2016150789
- Pollock JM, Tan H, Kraft RA, Whitlow CT, Burdette JH, Maldjian J. Arterial spin-labeled MR perfusion imaging: clinical applications. *Magn Reson Imaging Clin N Am*. 2009;17:315-338. doi:10.1016/j.mric.2009.01.008
- Telischak NA, Detre JA, Zaharchuk G. Arterial spin labeling MRI: clinical applications in the brain. *J Magn Reson Imaging*. 2015;41:1165-1180. doi:10.1002/jmri.24751
- Zaharchuk G. Arterial spin-labeled perfusion imaging in acute ischemic stroke. *Stroke*. 2014;45:1202-1207. doi:10.1161/STROKEAHA.113.003612
- Alsop DC, Detre JA, Golay X, et al. Recommended implementation of arterial spin-labeled perfusion MRI for clinical applications: a consensus of the ISMRM perfusion study group and the European consortium for ASL in dementia. *Magn Reson Med*. 2015;73:102-116. doi:10.1002/mrm.25197
- Wong EC, Buxton RB, Frank LR. Quantitative imaging of perfusion using a single subtraction (QUIPSS and QUIPSS II). *Magn Reson Med*. 1998;39:702-708. doi:10.1002/mrm.1910390506
- Qin Q, Alsop DC, Bolar DS, et al. Velocity-selective arterial spin labeling perfusion MRI: a review of the state of the art and recommendations for clinical implementation. *Magn Reson Med*. 2022;88:1528-1547. doi:10.1002/mrm.29371
- Alsop DC, Detre JA. Reduced transit-time sensitivity in non-invasive magnetic resonance imaging of human cerebral blood flow. *J Cereb Blood Flow Metab*. 1996;16:1236-1249. doi:10.1097/00004647-199611000-00019
- Thomas DL, Lythgoe MF, van der Weerd L, Ordidge RJ, Gadian DG. Regional variation of cerebral blood flow and arterial transit time in the Normal and Hypoperfused rat brain measured using continuous arterial spin labeling MRI. *J Cereb Blood Flow Metab*. 2006;26:274-282. doi:10.1038/sj.jcbfm.9600185
- Dai W, Shankaranarayanan A, Alsop DC. Volumetric measurement of perfusion and arterial transit delay using hadamard encoded continuous arterial spin labeling. *Magn Reson Med*. 2013;69:1014-1022. doi:10.1002/mrm.24335
- Günther M. Highly efficient accelerated acquisition of perfusion inflow series by Cycled Arterial Spin Labeling. In: *Proceedings of the 15th Annual Meeting of the ISMRM, Berlin, Germany.*; 2007:380.
- Woods JG, Chappell MA, Okell TW. Designing and comparing optimized pseudo-continuous arterial spin labeling

- protocols for measurement of cerebral blood flow. *Neuroimage*. 2020;223:117246. doi:10.1016/j.neuroimage.2020.117246
28. Francis ST, Bowtell R, Gowland PA. Modeling and optimization of look-locker spin labeling for measuring perfusion and transit time changes in activation studies taking into account arterial blood volume. *Magn Reson Med*. 2008;59:316-325. doi:10.1002/mrm.21442
 29. Buxton RB, Frank LR, Wong EC, Siewert B, Warach S, Edelman RR. A general kinetic model for quantitative perfusion imaging with arterial spin labeling. *Magn Reson Med*. 1998;40:383-396. doi:10.1002/mrm.1910400308
 30. Dai W, Robson PM, Shankaranarayanan A, Alsop DC. Reduced resolution transit delay prescan for quantitative continuous arterial spin labeling perfusion imaging. *Magn Reson Med*. 2012;67:1252-1265. doi:10.1002/mrm.23103
 31. Asllani I, Borogovac A, Brown TR. Regression algorithm correcting for partial volume effects in arterial spin labeling MRI. *Magn Reson Med*. 2008;60:1362-1371. doi:10.1002/mrm.21670
 32. Asllani I, Dharssi S, Pavol M, Lazar RL, Marshall RS. Measurement of hemodynamic parameters in carotid occlusive disease using partial volume corrected PCASL fMRI. *Proceedings of the 21st Annual Meeting of the ISMRM, Salt Lake City, USA*; 2013:2991
 33. Amemiya S, Watanabe Y, Takei N, et al. Arterial transit time-based multidelay combination strategy improves arterial spin labeling cerebral blood flow measurement accuracy in severe steno-occlusive diseases. *J Magn Reson Imaging*. 2022;55(1):178-187. doi:10.1002/jmri.27823
 34. Yun TJ, Sohn CH, Yoo RE, et al. Transit time corrected arterial spin labeling technique aids to overcome delayed transit time effect. *Neuroradiology*. 2018;60:255-265. doi:10.1007/s00234-017-1969-x
 35. Chalela JA, Alsop DC, Gonzalez-Atavales JB, Maldjian JA, Kassner SE, Detre JA. Magnetic resonance perfusion imaging in acute ischemic stroke using continuous arterial spin labeling. *Stroke*. 2000;31:680-687. doi:10.1161/01.STR.31.3.680
 36. Choi HJ, Sohn CH, You SH, et al. Can arterial spin-labeling with multiple Postlabeling delays predict cerebrovascular reserve? *Am J Neuroradiol*. 2018;39:84-90. doi:10.3174/ajnr.A5439
 37. Detre JA, Samuels OB, Alsop DC, Gonzalez-At JB, Kassner SE, Raps EC. Noninvasive magnetic resonance imaging evaluation of cerebral blood flow with acetazolamide challenge in patients with cerebrovascular stenosis. *J Magn Reson Imaging*. 1999;10:870-875. doi:10.1002/(SICI)1522-2586(199911)10:5<870::AID-JMRI36>3.0.CO;2-D
 38. Hendrikse J, van Osch MJP, Rutgers DR, et al. Internal carotid artery occlusion assessed at pulsed arterial spin-labeling perfusion MR imaging at multiple delay times. *Radiology*. 2004;233:899-904. doi:10.1148/radiol.2333031276
 39. Hu HH, Rusin JA, Peng R, et al. Multi-phase 3D arterial spin labeling brain MRI in assessing cerebral blood perfusion and arterial transit times in children at 3T. *Clin Imaging*. 2019;53:210-220. doi:10.1016/j.clinimag.2018.11.001
 40. Lin T, Lai Z, Lv Y, et al. Effective collateral circulation may indicate improved perfusion territory restoration after carotid endarterectomy. *Eur Radiol*. 2018;28:727-735. doi:10.1007/s00330-017-5020-8
 41. Lou X, Yu S, Scalzo F, et al. Multi-delay ASL can identify leptomeningeal collateral perfusion in endovascular therapy of ischemic stroke. *Oncotarget*. 2017;8:2437-2443. doi:10.18632/oncotarget.13898
 42. MacIntosh BJ, Marquardt L, Schulz UG, Jezzard P, Rothwell PM. Hemodynamic alterations in vertebrobasilar large artery disease assessed by arterial spin-labeling MR imaging. *Am J Neuroradiol*. 2012;33:1939-1944. doi:10.3174/ajnr.A3090
 43. Okazaki S, Griebel M, Gregori J, et al. Prediction of early reperfusion from repeated arterial spin labeling perfusion magnetic resonance imaging during intravenous thrombolysis. *Stroke*. 2016;47:247-250. doi:10.1161/STROKEAHA.115.011482
 44. Suman G, Rusin JA, Lebel RM, Hu HH. Multidelay arterial spin labeling MRI in the assessment of cerebral blood flow: preliminary clinical experience in pediatrics. *Pediatr Neurol*. 2020;103:79-83. doi:10.1016/j.pediatrneurol.2019.08.005
 45. Chappell M, MacIntosh BJ, Donahue MJ, Günther M, Jezzard P, Woolrich MW. Separation of macrovascular signal in multi-inversion time arterial spin labelling MRI. *Magn Reson Med*. 2010;63:1357-1365. doi:10.1002/mrm.22320
 46. Chappell MA, McConnell FAK, Golay X, et al. Partial volume correction in arterial spin labeling perfusion MRI: a method to disentangle anatomy from physiology or an analysis step too far? *Neuroimage*. 2021;238:118236. doi:10.1016/j.neuroimage.2021.118236
 47. Chappell MA, Woolrich MW, Kazan S, Jezzard P, Payne SJ, MacIntosh BJ. Modeling dispersion in arterial spin labeling: validation using dynamic angiographic measurements. *Magn Reson Med*. 2013;69:563-570. doi:10.1002/mrm.24260
 48. Gonzalez-At JB, Alsop DC, Detre JA. Cerebral perfusion and arterial transit time changes during task activation determined with continuous arterial spin labeling. *Magn Reson Med*. 2000;43:739-746.
 49. Chappell M, MacIntosh B, Okell T. *Introduction to Perfusion Quantification Using Arterial Spin Labelling*. Oxford University Press; 2017. doi:10.1093/oso/9780198793816.001.0001
 50. Dai W, Garcia D, De Bazelaire C, Alsop DC. Continuous flow-driven inversion for arterial spin labeling using pulsed radio frequency and gradient fields. *Magn Reson Med*. 2008;60:1488-1497. doi:10.1002/mrm.21790
 51. Edelman RR, Chen Q. EPISTAR MRI: multislice mapping of cerebral blood flow. *Magn Reson Med*. 1998;40:800-805. doi:10.1002/mrm.1910400603
 52. Kim SG. Quantification of relative cerebral blood flow change by flow-sensitive alternating inversion recovery (FAIR) technique: application to functional mapping. *Magn Reson Med*. 1995;34:293-301. doi:10.1002/mrm.1910340303
 53. Petersen ET, Lim T, Golay X. Model-free arterial spin labeling quantification approach for perfusion MRI. *Magn Reson Med*. 2006;55:219-232. doi:10.1002/mrm.20784
 54. Wong EC, Buxton RB, Frank LR. Implementation of quantitative perfusion imaging techniques for functional brain mapping using pulsed arterial spin labeling. *NMR Biomed*. 1997;10:237-249. doi:10.1002/(SICI)1099-1492(199706/08)10:4/5<237::AID-NBM475>3.0.CO;2-X [pii].
 55. Luh WM, Wong EC, Bandettini PA, Hyde JS. QUIPSS II with thin-slice TI1 periodic saturation: a method for improving accuracy of quantitative perfusion imaging using pulsed arterial spin labeling. *Magn Reson Med*. 1999;41:1246-1254. doi:10.1002/(SICI)1522-2594(199906)41:6<1246::AID-MRM22>3.0.CO;2-N

56. Wong EC, Cronin M, Wu WC, Inglis B, Frank LR, Liu TT. Velocity-selective arterial spin labeling. *Magn Reson Med*. 2006;55:1334-1341. doi:10.1002/mrm.20906
57. Guo J, Wong EC. Increased SNR efficiency in velocity selective arterial spin labeling using multiple velocity selective saturation modules (mm-VSASL). *Magn Reson Med*. 2015;74:694-705. doi:10.1002/mrm.25462
58. Bolar DS, Gagoski B, Orbach DB, et al. Comparison of CBF measured with combined velocity-selective arterial spin-labeling and pulsed arterial spin-labeling to blood flow patterns assessed by conventional angiography in pediatric Moyamoya. *Am J Neuroradiol*. 2019;40:1842-1849. doi:10.3174/ajnr.A6262
59. Qiu M, Paul Maguire R, Arora J, et al. Arterial transit time effects in pulsed arterial spin labeling CBF mapping: insight from a PET and MR study in normal human subjects. *Magn Reson Med*. 2010;63:374-384. doi:10.1002/mrm.22218
60. Zhao L, Vidorreta M, Soman S, Detre JA, Alsop DC. Improving the robustness of pseudo-continuous arterial spin labeling to off-resonance and pulsatile flow velocity. *Magn Reson Med*. 2017;78:1342-1351. doi:10.1002/mrm.26513
61. Sokolska M, Bainbridge A, Rojas-Villabona A, Golay X, Thomas DL. Effect of labelling plane angulation and position on labelling efficiency and cerebral blood flow quantification in pseudo-continuous arterial spin labelling. *Magn Reson Imaging*. 2019;59:61-67. doi:10.1016/j.mri.2019.02.007
62. Woods JG, Chappell MA, Okell TW. A general framework for optimizing arterial spin labeling MRI experiments. *Magn Reson Med*. 2019;81:2474-2488. doi:10.1002/mrm.27580
63. Qin Q, Huang AJ, Hua J, Desmond JE, Stevens RD, van Zijl PCM. Three-dimensional whole-brain perfusion quantification using pseudo-continuous arterial spin labeling MRI at multiple post-labeling delays: accounting for both arterial transit time and impulse response function. *NMR Biomed*. 2014;27:116-128. doi:10.1002/nbm.3040
64. Borogovac A, Habeck C, Small SA, Asllani I. Mapping brain function using a 30-day interval between baseline and activation: a novel arterial spin labeling fMRI approach. *J Cereb Blood Flow Metab*. 2010;30:1721-1733. doi:10.1038/jcbfm.2010.89
65. Johnston ME, Lu K, Maldjian JA, Jung Y. Multi-TI arterial spin labeling MRI with variable TR and bolus duration for cerebral blood flow and arterial transit time mapping. *IEEE Trans Med Imaging*. 2015;34:1392-1402. doi:10.1109/TMI.2015.2395257
66. Zhao L, Fielden SW, Feng X, Wintermark M, Mugler JP, Meyer CH. Rapid 3D dynamic arterial spin labeling with a sparse model-based image reconstruction. *Neuroimage*. 2015;121:205-216. doi:10.1016/j.neuroimage.2015.07.018
67. Teeuwisse WM, Schmid S, Ghariq E, Veer IM, van Osch MJP. Time-encoded pseudocontinuous arterial spin labeling: basic properties and timing strategies for human applications. *Magn Reson Med*. 2014;72:1712-1722. doi:10.1002/mrm.25083
68. Wells JA, Lythgoe MF, Gadian DG, Ordidge RJ, Thomas DL. In vivo hadamard encoded continuous arterial spin labeling (H-CASL). *Magn Reson Med*. 2010;63:1111-1118. doi:10.1002/mrm.22266
69. Hall M. Chapter 14 Hadamard matrices. *Combinatorial Theory*. John Wiley & Sons, Ltd; 1988:238-263. doi:10.1002/9781118032862.ch14
70. Guo J, Holdsworth SJ, Fan AP, et al. Comparing accuracy and reproducibility of sequential and Hadamard-encoded multidelay pseudocontinuous arterial spin labeling for measuring cerebral blood flow and arterial transit time in healthy subjects: a simulation and in vivo study. *J Magn Reson Imaging*. 2018;47:1119-1132. doi:10.1002/jmri.25834
71. von Samson-Himmelstjerna F, Madai VI, Sobesky J, Guenther M. Walsh-ordered hadamard time-encoded pseudocontinuous ASL (WH pCASL). *Magn Reson Med*. 2016;76:1814-1824. doi:10.1002/mrm.26078
72. Cohen AD, Agarwal M, Jagra AS, et al. Longitudinal reproducibility of MR perfusion using 3D Pseudocontinuous arterial spin labeling with Hadamard-encoded multiple Postlabeling delays. *J Magn Reson Imaging*. 2019;jmri.27007;51:1846-1853. doi:10.1002/jmri.27007
73. Neumann K, Schidlowski M, Günther M, Stöcker T, Düzel E. Reliability and reproducibility of Hadamard encoded pseudo-continuous arterial spin labeling in healthy elderly. *Front Neurosci*. 2021;15:1029. doi:10.3389/fnins.2021.711898
74. Günther M, Bock M, Schad LR. Arterial spin labeling in combination with a look-locker sampling strategy: inflow turbo-sampling EPI-FAIR (ITS-FAIR). *Magn Reson Med*. 2001;46:974-984. doi:10.1002/mrm.1284
75. van der Plas MCE, Teeuwisse WM, Schmid S, Chappell M, van Osch MJP. High temporal resolution arterial spin labeling MRI with whole-brain coverage by combining time-encoding with look-locker and simultaneous multi-slice imaging. *Magn Reson Med*. 2019;81:3734-3744. doi:10.1002/mrm.27692
76. Bokkers RPH, van Laar PJ, van de Ven KCC, Kapelle LJ, Klijn CJM, Hendrikse J. Arterial spin-labeling MR imaging measurements of timing parameters in patients with a carotid artery occlusion. *Am J Neuroradiol*. 2008;29:1698-1703. doi:10.3174/ajnr.A1232
77. Paschoal AM, Leoni RF, Foerster BU, dos Santos AC, Pontes-Neto OM, Paiva FF. Contrast optimization in arterial spin labeling with multiple post-labeling delays for cerebrovascular assessment. *Magn Reson Mater Phys Biol Med*. 2020;34:119-131. doi:10.1007/s10334-020-00883-z
78. Okell TW, Chappell MA, Jezzard P. A theoretical framework for quantifying blood volume flow rate from dynamic angiographic data and application to vessel-encoded arterial spin labeling MRI. *Med Image Anal*. 2013;17:1025-1036. doi:10.1016/j.media.2013.06.005
79. Fujima N, Kudo K, Yoshida D, et al. Arterial spin labeling to determine tumor viability in head and neck cancer before and after treatment: ASL for head and neck cancer. *J Magn Reson Imaging*. 2014;40:920-928. doi:10.1002/jmri.24421
80. Yoshiura T, Hiwatashi A, Yamashita K, et al. Simultaneous measurement of arterial transit time, arterial blood volume, and cerebral blood flow using arterial spin-labeling in patients with Alzheimer disease. *Am J Neuroradiol*. 2009;30:1388-1393. doi:10.3174/ajnr.A1562
81. Lee Y, Kim T. Assessment of hypertensive cerebrovascular alterations with multiband look-locker arterial spin labeling: whole brain perfusion dynamics with MB LL-FAIR. *J Magn Reson Imaging*. 2018;47:663-672. doi:10.1002/jmri.25812
82. Zhang K, Yun SD, Shah NJ. Triple readout slices in multi time-point pCASL using multiband look-locker EPI. Hendrikse J, ed. *PloS One*. 2015;10:e0141108. doi:10.1371/journal.pone.0141108
83. Lahiri A, Fessler JA, Hernandez-Garcia L. Optimizing MRF-ASL scan design for precise quantification of brain

- hemodynamics using neural network regression. *Magn Reson Med.* 2020;83:1979-1991. doi:10.1002/mrm.28051
84. Su P, Fan H, Liu P, et al. MR fingerprinting ASL: sequence characterization and comparison with dynamic susceptibility contrast (DSC) MRI. *NMR Biomed.* 2020;33:1-13. doi:10.1002/nbm.4202
 85. Su P, Mao D, Liu P, et al. Multiparametric estimation of brain hemodynamics with MR fingerprinting ASL. *Magn Reson Med.* 2017;78:1812-1823. doi:10.1002/mrm.26587
 86. Wright KL, Jiang Y, Ma D, et al. Estimation of perfusion properties with MR fingerprinting arterial spin labeling. *Magn Reson Imaging.* 2018;50:68-77. doi:10.1016/j.mri.2018.03.011
 87. Hernandez-Garcia L, Aramendia-Vidaurreta V, Bolar DS, et al. Recent technical developments in ASL: a review of the state of the art. *Magn Reson Med.* 2022;88:2021-2042. doi:10.1002/mrm.29381
 88. Cramer H. *Mathematical Methods of Statistics*. 9th ed. Princeton University Press; 1946 <https://www.jstor.org/stable/2280199?origin=crossref>
 89. Bladt P, Dekker AJ, Clement P, Achten E, Sijbers J. The costs and benefits of estimating T1 of tissue alongside cerebral blood flow and arterial transit time in pseudo-continuous arterial spin labeling. *NMR Biomed.* 2019;November 2018:1-17. doi:10.1002/nbm.4182
 90. Gardener AG, Jezzard P. Investigating white matter perfusion using optimal sampling strategy arterial spin labeling at 7 tesla. *Magn Reson Med.* 2015;73:2243-2248. doi:10.1002/mrm.25333
 91. Owen D, Melbourne A, Thomas D, De Vita E, Rohrer J, Ourselin S. Optimisation of arterial spin labelling using Bayesian experimental design. In: Ourselin S, Joskowicz L, Sabuncu M, Unal G, Wells W, eds. *Medical Image Computing and Computer-Assisted Intervention – MICCAI 2016*. Lecture Notes in Computer Science. Vol 9902. Springer; 2016:511-518. doi:10.1007/978-3-319-46726-9_59
 92. Sanches J, Sousa I, Figueiredo P. Bayesian fisher information criterion for sampling optimization in ASL-MRI. *2010 IEEE International Symposium on Biomedical Imaging: from Nano to Macro, Rotterdam, Netherlands*. IEEE; 2010:880-883. doi:10.1109/ISBI.2010.5490127
 93. Santos N, Sanches JM, Sousa I, Figueiredo P. Optimal sampling and estimation in PASL perfusion imaging. *IEEE Trans Biomed Eng.* 2011;58:3165-3174. doi:10.1109/TBME.2011.2164916
 94. Xie J, Clare S, Gallichan D, Gunn RN, Jezzard P. Real-time adaptive sequential design for optimal acquisition of arterial spin labeling MRI data. *Magn Reson Med.* 2010;64:203-210. doi:10.1002/mrm.22398
 95. Xie J, Gallichan D, Gunn RN, Jezzard P. Optimal design of pulsed arterial spin labeling MRI experiments. *Magn Reson Med.* 2008;59:826-834. doi:10.1002/mrm.21549
 96. Zhang LX, Woods JG, Okell TW, Chappell MA. Examination of optimized protocols for pCASL: sensitivity to macrovascular contamination, flow dispersion, and prolonged arterial transit time. *Magn Reson Med.* 2021;86:2208-2219. doi:10.1002/mrm.28839
 97. Zhao L, Meyer CH. Optimal PLD design and maximum likelihood CBF estimation for dynamic PCASL with Rician noise. *Proceedings of the 21st Annual Meeting of the ISMRM, Salt Lake City, USA*; 2013:2164.
 98. Zhao L, Meyer CH. Optimal kinetic PASL design and CBF estimation with low SNR and Rician noise. *Proceedings of the 20th Annual Meeting of the ISMRM, Melbourne, Australia*; 2012:3494.
 99. Dixon WT, Sardashti M, Castillo M, Stomp GP. Multiple inversion recovery reduces static tissue signal in angiograms. *Magn Reson Med.* 1991;18:257-268. doi:10.1002/mrm.1910180202
 100. Günther M, Oshio K, Feinberg DA. Single-shot 3D imaging techniques improve arterial spin labeling perfusion measurements. *Magn Reson Med.* 2005;54:491-498. doi:10.1002/mrm.20580
 101. Maleki N, Dai W, Alsop DC. Optimization of background suppression for arterial spin labeling perfusion imaging. *Magn Reson Mater Phys Biol Med.* 2012;25:127-133. doi:10.1007/s10334-011-0286-3
 102. Mani S, Pauly J, Conolly S, Meyer C, Nishimura D. Background suppression with multiple inversion recovery nulling: applications to projective angiography. *Magn Reson Med.* 1997;37:898-905. doi:10.1002/mrm.1910370615
 103. Ye FQ, Frank JA, Weinberger DR, McLaughlin AC. Noise reduction in 3D perfusion imaging by attenuating the static signal in arterial spin tagging (ASSIST). *Magn Reson Med.* 2000;44:92-100. doi:10.1002/1522-2594(200007)44:1<92::AID-MRM14>3.0.CO;2-M
 104. Garcia DM, Duhamel G, Alsop DC. Efficiency of inversion pulses for background suppressed arterial spin labeling. *Magn Reson Med.* 2005;54:366-372. doi:10.1002/mrm.20556
 105. Vidorreta M, Wang Z, Rodriguez I, Pastor MA, Detre JA, Fernández-Seara MA. Comparison of 2D and 3D single-shot ASL perfusion fMRI sequences. *Neuroimage.* 2013;66:662-671. doi:10.1016/j.neuroimage.2012.10.087
 106. Dai W, Varma G, Scheidegger R, Alsop DC. Quantifying fluctuations of resting state networks using arterial spin labeling perfusion MRI. *J Cereb Blood Flow Metab.* 2016;36:463-473. doi:10.1177/0271678X15615339
 107. Zhao L, Alsop DC, Detre JA, Dai W. Global fluctuations of cerebral blood flow indicate a global brain network independent of systemic factors. *J Cereb Blood Flow Metab.* 2019;39:302-312. doi:10.1177/0271678X17726625
 108. Shin DD, Liu HL, Wong EC, Liu TT. Effect of background suppression on CBF quantitation in pseudo continuous arterial spin labeling. *Proceedings of the 19th Annual Meeting of the ISMRM, Montreal, Canada*; 2011:2101.
 109. Ye FQ, Mattay VS, Jezzard P, Frank JA, Weinberger DR, McLaughlin AC. Correction for vascular artifacts in cerebral blood flow values measured by using arterial spin tagging techniques. *Magn Reson Med.* 1997;37:226-235. doi:10.1002/mrm.1910370215
 110. Zaharchuk G. Arterial spin labeling for acute stroke: practical considerations. *Transl Stroke Res.* 2012;3:228-235. doi:10.1007/s12975-012-0159-8
 111. Vidyasagar R, Abernethy L, Pizer B, Avula S, Parkes LM. Quantitative measurement of blood flow in paediatric brain tumours—a comparative study of dynamic susceptibility contrast and multi time-point arterial spin labelled MRI. *Br J Radiol.* 2016;89:20150624. doi:10.1259/bjr.20150624
 112. Feinberg D, Ramann S, Günther M. Evaluation of new ASL 3D GRASE sequences using parallel imaging, segmented and interleaved k-space at 3T with 12- and 32-channel coils. *Proceedings of the 17th Annual Meeting of the ISMRM, Honolulu, USA*; 2009:623.

113. Fernández-Seara MA, Wang Z, Wang J, et al. Continuous arterial spin labeling perfusion measurements using single shot 3D GRASE at 3 T. *Magn Reson Med*. 2005;54:1241-1247. doi:10.1002/mrm.20674
114. Vidorreta M, Wang Z, Chang YV, Wolk DA, Fernández-Seara MA, Detre JA. Whole-brain background-suppressed pCASL MRI with 1D-accelerated 3D RARE stack-of-spirals readout. *PloS One*. 2017;12(8):e0183762. doi:10.1371/journal.pone.0183762
115. Boland M, Stirnberg R, Pracht ED, et al. Accelerated 3D-GRASE imaging improves quantitative multiple post labeling delay arterial spin labeling. *Magn Reson Med*. 2018;80:2475-2484. doi:10.1002/mrm.27226
116. Chang YV, Vidorreta M, Wang Z, Detre JA. 3D-accelerated, stack-of-spirals acquisitions and reconstruction of arterial spin labeling MRI. *Magn Reson Med*. 2017;78:1405-1419. doi:10.1002/mrm.26549
117. Feinberg DA, Beckett A, Chen L. Arterial spin labeling with simultaneous multi-slice echo planar imaging. *Magn Reson Med*. 2013;70:1500-1506. doi:10.1002/mrm.24994
118. Kim T, Shin W, Zhao T, Beall EB, Lowe MJ, Bae KT. Whole brain perfusion measurements using arterial spin labeling with multiband acquisition. *Magn Reson Med*. 2013;70:1653-1661. doi:10.1002/mrm.24880
119. Shao X, Wang Y, Moeller S, Wang DJJ. A constrained slice-dependent background suppression scheme for simultaneous multislice pseudo-continuous arterial spin labeling: a constrained slice-dependent BS scheme for SMS pCASL. *Magn Reson Med*. 2018;79:394-400. doi:10.1002/mrm.26643
120. Suzuki Y, Okell TW, Chappell MA, van Osch MJP. A framework for motion correction of background suppressed arterial spin labeling perfusion images acquired with simultaneous multi-slice EPI. *Magn Reson Med*. 2019;81:1553-1565. doi:10.1002/mrm.27499
121. Fan H, Mutsaerts HJMM, Anazodo U, et al. ISMRM Open Science Initiative for Perfusion Imaging (OSIPI): ASL pipeline inventory. *Magn Reson Med*. 2024;91(5):1787-1802. doi:10.1002/mrm.29869
122. Detre JA, Leigh JS, Williams DS, Koretsky AP. Perfusion imaging. *Magn Reson Med*. 1992;23:37-45. doi:10.1002/mrm.1910230106
123. Kwong KK, Chesler DA, Weisskoff RM, et al. Mr perfusion studies with t1-weighted echo planar imaging. *Magn Reson Med*. 1995;34:878-887. doi:10.1002/mrm.1910340613
124. Kwong KK, Belliveau JW, Chesler DA, et al. Dynamic magnetic resonance imaging of human brain activity during primary sensory stimulation. *Proc Natl Acad Sci*. 1992;89:5675-5679. doi:10.1073/pnas.89.12.5675
125. Kety SS, Schmidt CF. The nitrous oxide method for the quantitative determination of cerebral blood flow in man: theory, procedure and normal values. *J Clin Invest*. 1948;27:476-483. doi:10.1172/JCI101994
126. Çavuşoğlu M, Pfeuffer J, Uğurbil K, Uludağ K. Comparison of pulsed arterial spin labeling encoding schemes and absolute perfusion quantification. *Magn Reson Imaging*. 2009;27:1039-1045. doi:10.1016/j.mri.2009.04.002
127. Fazlollahi A, Bourgeat P, Liang X, et al. Reproducibility of multiphase pseudo-continuous arterial spin labeling and the effect of post-processing analysis methods. *Neuroimage*. 2015;117:191-201. doi:10.1016/j.neuroimage.2015.05.048
128. Pinto J, Chappell MA, Okell TW, et al. Calibration of arterial spin labeling data—potential pitfalls in post-processing. *Magn Reson Med*. 2020;83:1222-1234. doi:10.1002/mrm.28000
129. Parkes LM, Tofts PS. Improved accuracy of human cerebral blood perfusion measurements using arterial spin labeling: accounting for capillary water permeability. *Magn Reson Med*. 2002;48:27-41. doi:10.1002/mrm.10180
130. Juttukonda MR, Li B, Almaktoom R, et al. Characterizing cerebral hemodynamics across the adult lifespan with arterial spin labeling MRI data from the human connectome project-aging. *Neuroimage*. 2021;230:117807. doi:10.1016/j.neuroimage.2021.117807
131. Chappell MA, Groves AR, Whitcher B, Woolrich MW. Variational Bayesian inference for a nonlinear forward model. *IEEE Trans Signal Process*. 2009;57:223-236. doi:10.1109/TSP.2008.2005752
132. Sousa I, Vilela P, Figueiredo P. Reproducibility of the quantification of arterial and tissue contributions in multiple post-labeling delay arterial spin labeling. *J Magn Reson Imaging*. 2014;40:1453-1462. doi:10.1002/jmri.24493
133. Paschoal AM, Woods JG, Pinto J, et al. Reproducibility of arterial spin labeling cerebral blood flow image processing: A report of the ISMRM open science initiative for perfusion imaging (OSIPI) and the ASL MRI challenge. *Magn Reson Med*. 2024. doi:10.1002/mrm.30081
134. Fan H, Su P, Huang J, Liu P, Lu H. Multi-band MR fingerprinting (MRF) ASL imaging using artificial-neural-network trained with high-fidelity experimental data. *Magn Reson Med*. 2021;85:1974-1985. doi:10.1002/mrm.28560
135. Guo J, Gong E, Fan AP, Goubran M, Khalighi MM, Zaharchuk G. Predicting 15O-water PET cerebral blood flow maps from multi-contrast MRI using a deep convolutional neural network with evaluation of training cohort bias. *J Cereb Blood Flow Metab*. 2020;40:2240-2253. doi:10.1177/0271678X19888123
136. Zhang Q, Su P, Chen Z, et al. Deep learning-based MR fingerprinting ASL ReconStruction (DeepMARS). *Magn Reson Med*. 2020;84:1024-1034. doi:10.1002/mrm.28166
137. Lu H, Clingman C, Golay X, van Zijl PCM. Determining the longitudinal relaxation time (T1) of blood at 3.0 tesla. *Magn Reson Med*. 2004;52:679-682. doi:10.1002/mrm.20178
138. Li W, Liu P, Lu H, Strouse JJ, van Zijl PCM, Qin Q. Fast measurement of blood T1 in the human carotid artery at 3T: accuracy, precision, and reproducibility: fast measurement of arterial blood T1 at 3T. *Magn Reson Med*. 2017;77:2296-2302. doi:10.1002/mrm.26325
139. Qin Q, Strouse JJ, van Zijl PCM. Fast measurement of blood T1 in the human jugular vein at 3 tesla. *Magn Reson Med*. 2011;65:1297-1304. doi:10.1002/mrm.22723
140. Varela M, Hajnal JV, Petersen ET, Golay X, Merchant N, Larkman DJ. A method for rapid *in vivo* measurement of blood T₁: a method for rapid *in vivo* measurement of blood T₁. *NMR Biomed*. 2011;24:80-88. doi:10.1002/nbm.1559
141. Wu WC, Jain V, Li C, et al. In vivo venous blood T1 measurement using inversion recovery true-FISP in children and adults. *Magn Reson Med*. 2010;64:1140-1147. doi:10.1002/mrm.22484
142. Bluemke E, Stride E, Bulte DP. A general model to calculate the spin-lattice relaxation rate (R1) of blood, accounting for hematocrit, oxygen saturation, oxygen partial pressure,

- and magnetic field strength under Hyperoxic conditions. *J Magn Reson Imaging*. 2021;jmri.27938;55:1428-1439. doi:10.1002/jmri.27938
143. Hales PW, Kirkham FJ, Clark CA. A general model to calculate the spin-lattice (T_1) relaxation time of blood, accounting for haematocrit, oxygen saturation and magnetic field strength. *J Cereb Blood Flow Metab*. 2016;36:370-374. doi:10.1177/0271678X15605856
 144. Li W, Grgac K, Huang A, Yadav N, Qin Q, van Zijl PCM. Quantitative theory for the longitudinal relaxation time of blood water. *Magn Reson Med*. 2016;76:270-281. doi:10.1002/mrm.25875
 145. Václavů L, van der Land V, Heijtel DFR, et al. In vivo T_1 of blood measurements in children with sickle cell disease improve cerebral blood flow quantification from arterial spin-labeling MRI. *Am J Neuroradiol*. 2016;37:1727-1732. doi:10.3174/ajnr.A4793
 146. Siero JCW, Strother MK, Faraco CC, Hoogduin H, Hendrikse J, Donahue MJ. In vivo quantification of hyperoxic arterial blood water T_1 . *NMR Biomed*. 2015;28:1518-1525. doi:10.1002/nbm.3411
 147. Bladt P, Van Osch MJP, Clement P, Achten E, Sijbers J, den Dekker AJ. Supporting measurements or more averages? How to quantify cerebral blood flow most reliably in 5 minutes by arterial spin labeling. *Magn Reson Med*. 2020;84:2523-2536. doi:10.1002/mrm.28314
 148. Debacker CS, Daoust A, Köhler S, Voiron J, Warnking JM, Barbier EL. Impact of tissue T_1 on perfusion measurement with arterial spin labeling. *Magn Reson Med*. 2017;77:1656-1664. doi:10.1002/mrm.26255
 149. Marques JP, Kober T, Krueger G, van der Zwaag W, Van de Moortele PF, Gruetter R. MP2RAGE, a self bias-field corrected sequence for improved segmentation and T_1 -mapping at high field. *Neuroimage*. 2010;49:1271-1281. doi:10.1016/j.neuroimage.2009.10.002
 150. Wansapura JP, Holland SK, Dunn RS, Ball WS. NMR relaxation times in the human brain at 3.0 tesla. *J Magn Reson Imaging JMRI*. 1999;9:531-538.
 151. Parkes LM. Quantification of cerebral perfusion using arterial spin labeling: two-compartment models. *J Magn Reson Imaging*. 2005;22:732-736. doi:10.1002/jmri.20456
 152. Dickie BR, Parker GJ, Parkes LM. Measuring water exchange across the blood-brain barrier using MRI. *Prog Nucl Magn Reson Spectrosc*. 2020;116:19-39. doi:10.1016/j.pnmrs.2019.09.002
 153. Gregori J, Schuff N, Kern R, Günther M. T_2 -based arterial spin labeling measurements of blood to tissue water transfer in human brain. *J Magn Reson Imaging*. 2013;37:332-342. doi:10.1002/jmri.23822
 154. Wells JA, Siow B, Lythgoe MF, Thomas DL. Measuring biexponential transverse relaxation of the ASL signal at 9.4 T to estimate arterial oxygen saturation and the time of exchange of labeled blood water into cortical brain tissue. *J Cereb Blood Flow Metab*. 2013;33:215-224. doi:10.1038/jcbfm.2012.156
 155. Schollenberger J, Osborne NH, Hernandez-Garcia L, Figueroa CA. A combined computational fluid dynamics and arterial spin labeling MRI modeling strategy to quantify patient-specific cerebral hemodynamics in cerebrovascular occlusive disease. *Front Bioeng Biotechnol*. 2021;9. doi:10.3389/fbioe.2021.722445.
 156. Hrabe J, Lewis DP. Two analytical solutions for a model of pulsed arterial spin labeling with randomized blood arrival times. *J Magn Reson*. 2004;167:49-55. doi:10.1016/j.jmr.2003.11.002
 157. Ozyurt O, Dincer A, Acquitter C. A modified version of Hrabe-Lewis model to account dispersion of labeled bolus in arterial spin labeling. *Proceedings of the 18th Annual Meeting of the ISMRM, Stockholm, Sweden*; 2010:4065.
 158. Gallichan D, Jezzard P. Modeling the effects of dispersion and pulsatility of blood flow in pulsed arterial spin labeling. *Magn Reson Med*. 2008;60:53-63. doi:10.1002/mrm.21654
 159. Okell TW, Chappell MA, Schulz UG, Jezzard P. A kinetic model for vessel-encoded dynamic angiography with arterial spin labeling. *Magn Reson Med*. 2012;68:969-979. doi:10.1002/mrm.23311
 160. van der Plas MCE, Craig M, Schmid S, Chappell MA, van Osch MJP. Validation of the estimation of the macrovascular contribution in multi-timepoint arterial spin labeling MRI using a 2-component kinetic model. *Magn Reson Med*. 2021;87:85-101. doi:10.1002/mrm.28960
 161. Mehta RR, Chappell MA. Quantification of errors in cerebral blood flow measurements due to dispersion in arterial spin labelling. *2015 37th Annual International Conference of the IEEE Engineering in Medicine and Biology Society (EMBC)*. IEEE; 2015:7917-7920. doi:10.1109/EMBC.2015.7320228
 162. Pinto J, Blockley NP, Harkin JW, Bulte DP. Modelling spatiotemporal dynamics of cerebral blood flow using multiple-timepoint arterial spin labelling MRI. *Front Physiol*. 2023;14:14. doi:10.3389/fphys.2023.1142359
 163. Chappell MA, Groves AR, MacIntosh BJ, Donahue MJ, Jezzard P, Woolrich MW. Partial volume correction of multiple inversion time arterial spin labeling MRI data. *Magn Reson Med*. 2011;65:1173-1183. doi:10.1002/mrm.22641
 164. Liu TT, Wong EC. A signal processing model for arterial spin labeling functional MRI. *Neuroimage*. 2005;24:207-215. doi:10.1016/j.neuroimage.2004.09.047
 165. Frost R, Hess AT, Okell TW, et al. Prospective motion correction and selective reacquisition using volumetric navigators for vessel-encoded arterial spin labeling dynamic angiography. *Magn Reson Med*. 2016;76:1420-1430. doi:10.1002/mrm.26040
 166. Zun Z, Shankaranarayanan A, Zaharchuk G. Pseudocontinuous arterial spin labeling with prospective motion correction (PCASL-PROMO). *Magn Reson Med*. 2014;72:1049-1056. doi:10.1002/mrm.25024
 167. Gallichan D, Marques JP, Gruetter R. Retrospective correction of involuntary microscopic head movement using highly accelerated fat image navigators (3D FatNavs) at 7T. *Magn Reson Med*. 2016;75:1030-1039. doi:10.1002/mrm.25670
 168. Highton J, De Vita E, Schott JM, Thomas DL. Retrospective motion correction of multi-shot 3D GRASE arterial spin labelling using ESPIRiT reconstruction. *Proceedings of the 29th Annual Meeting of the ISMRM, Virtual*; 2021:2727.
 169. Huber J, Hoinkiss DC, Günther M. Joint estimation and correction of motion and geometric distortion in segmented arterial spin labeling. *Magn Reson Med*. 2021;mrm.29083;87:1876-1885. doi:10.1002/mrm.29083
 170. Rigie D, Vahle T, Zhao T, et al. Cardiorespiratory motion-tracking via self-refocused rosette navigators. *Magn Reson Med*. 2019;81(5):2947-212. doi:10.1002/mrm.27609

171. Suzuki Y, Okell T, Woods JG, Chappell M. A novel motion correction for ASL-fMRI with multi-PLD: non-parametric gaussian processes prediction of background suppression. *Proceedings of the 28th Annual Meeting of the ISMRM, Virtual*; 2020:3868.
172. Wang Z. Improving cerebral blood flow quantification for arterial spin labeled perfusion MRI by removing residual motion artifacts and global signal fluctuations. *Magn Reson Imaging*. 2012;30:1409-1415. doi:10.1016/j.mri.2012.05.004
173. Dolui S, Fan AP, Zhao MY, Nasrallah IM, Zaharchuk G, Detre JA. Reliability of arterial spin labeling derived cerebral blood flow in periventricular white matter. *Neuroimage Rep*. 2021;1:100063. doi:10.1016/j.ynirp.2021.100063
174. Skurdal MJ, Bjørnerud A, van Osch MJP, Nordhøy W, Lagopoulos J, Groote IR. Voxel-wise perfusion assessment in cerebral white matter with PCASL at 3T; is it possible and how long does it take? *PLoS One*. 2015;10:e0135596. doi:10.1371/journal.pone.0135596
175. van Gelderen P, de Zwart JA, Duyn JH. Pitfalls of MRI measurement of white matter perfusion based on arterial spin labeling. *Magn Reson Med*. 2008;59:788-795. doi:10.1002/mrm.21515
176. van Osch MJP, Teeuwisse WM, van Walderveen MAA, Hendrikse J, Kies DA, van Buchem MA. Can arterial spin labeling detect white matter perfusion signal? *Magn Reson Med*. 2009;62:165-173. doi:10.1002/mrm.22002
177. Zhang X, Ronen I, Kan HE, Teeuwisse WM, van Osch MJP. Time-efficient measurement of multi-phase arterial spin labeling MR signal in white matter. *NMR Biomed*. 2016;29:1519-1525. doi:10.1002/nbm.3603
178. Liu P, De Vis JB, Lu H. Cerebrovascular reactivity (CVR) MRI with CO₂ challenge: a technical review. *Neuroimage*. 2019;187:104-115. doi:10.1016/j.neuroimage.2018.03.047
179. Pinto J, Bright MG, Bulte DP, Figueiredo P. Cerebrovascular reactivity mapping without gas challenges: a methodological guide. *Front Physiol*. 2021;11:608475. doi:10.3389/fphys.2020.608475
180. Solis-Barquero SM, Echeverria-Chasco R, Calvo-Imirizaldu M, et al. Breath-hold induced cerebrovascular reactivity measurements using optimized Pseudocontinuous arterial spin labeling. *Front Physiol*. 2021;12:12. doi:10.3389/fphys.2021.621720
181. Markus H, Cullinane M. Severely impaired cerebrovascular reactivity predicts stroke and TIA risk in patients with carotid artery stenosis and occlusion. *Brain*. 2001;124:457-467. doi:10.1093/brain/124.3.457
182. Yonas H, Smith HA, Durham SR, Pentheny SL, Johnson DW. Increased stroke risk predicted by compromised cerebral blood flow reactivity. *J Neurosurg*. 1993;79:483-489. doi:10.3171/jns.1993.79.4.0483
183. Hund-Georgiadis M, Zysset S, Naganawa S, Norris DG, von Cramon DY. Determination of cerebrovascular reactivity by means of fMRI signal changes in cerebral microangiopathy: a correlation with morphological abnormalities. *Cerebrovasc Dis*. 2003;16:158-165. doi:10.1159/000070596
184. Conijn MMA, Hoogduin JM, van der Graaf Y, Hendrikse J, Luijten PR, Geerlings MI. Microbleeds, lacunar infarcts, white matter lesions and cerebrovascular reactivity — a 7T study. *Neuroimage*. 2012;59:950-956. doi:10.1016/j.neuroimage.2011.08.059
185. Jay J, Pillai DZ. Clinical utility of cerebrovascular reactivity mapping in patients with low grade gliomas. *World J Clin Oncol*. 2011;2:397-403. doi:10.5306/wjco.v2.i12.397
186. Zacà D, Jovicich J, Nadar SR, Voyvodic JT, Pillai JJ. Cerebrovascular reactivity mapping in patients with low grade gliomas undergoing presurgical sensorimotor mapping with BOLD fMRI. *J Magn Reson Imaging*. 2014;40:383-390. doi:10.1002/jmri.24406
187. Iranmahboob A, Peck KK, Brennan NP, et al. Vascular reactivity maps in patients with gliomas using breath-holding BOLD fMRI. *J Neuroimaging*. 2016;26:232-239. doi:10.1111/jon.12278
188. Vicenzini E, Ricciardi MC, Altieri M, et al. Cerebrovascular reactivity in degenerative and vascular dementia: a transcranial doppler study. *Eur Neurol*. 2007;58:84-89. doi:10.1159/000103642
189. Silvestrini M, Pasqualetti P, Baruffaldi R, et al. Cerebrovascular reactivity and cognitive decline in patients with Alzheimer disease. *Stroke*. 2006;37:1010-1015. doi:10.1161/01.STR.0000206439.62025.97
190. Chan ST, Mercaldo ND, Kwong KK, Hersch SM, Rosas HD. Impaired cerebrovascular reactivity in Huntington's disease. *Front Physiol*. 2021;12:12. doi:10.3389/fphys.2021.663898
191. Pelizzari L, Laganà MM, Rossetto F, et al. Cerebral blood flow and cerebrovascular reactivity correlate with severity of motor symptoms in Parkinson's disease. *Ther Adv Neurol Disord*. 2019;12:1756286419838354. doi:10.1177/1756286419838354
192. Donahue MJ, Faraco CC, Strother MK, et al. Bolus arrival time and cerebral blood flow responses to hypercarbia. *J Cereb Blood Flow Metab*. 2014;34:1243-1252. doi:10.1038/jcbfm.2014.81
193. Ho YCL, Petersen ET, Zimine I, Golay X. Similarities and differences in arterial responses to hypercapnia and visual stimulation. *J Cereb Blood Flow Metab*. 2011;31:560-571. doi:10.1038/jcbfm.2010.126
194. Zhao MY, Václavů L, Petersen ET, et al. Quantification of cerebral perfusion and cerebrovascular reserve using turbo-QUASAR arterial spin labeling MRI. *Magn Reson Med*. 2020;83:731-748. doi:10.1002/mrm.27956
195. Wang R, Yu S, Alger JR, et al. Multi-delay arterial spin labeling perfusion MRI in moyamoya disease – comparison with CT perfusion imaging. *Eur Radiol*. 2014;24:1135-1144. doi:10.1007/s00330-014-3098-9
196. Federau C, Christensen S, Zun Z, et al. Cerebral blood flow, transit time, and apparent diffusion coefficient in moyamoya disease before and after acetazolamide. *Neuroradiology*. 2017;59:5-12. doi:10.1007/s00234-016-1766-y
197. Amemiya S, Takao H, Watanabe Y, et al. Reliability and sensitivity to longitudinal CBF changes in steno-occlusive diseases: ASL versus 123I-IMP-SPECT. *J Magn Reson Imaging*. 2022;55:1723-1732. doi:10.1002/jmri.27996
198. Zhao MY, Armindo RD, Gauden AJ, et al. Revascularization improves vascular hemodynamics – a study assessing cerebrovascular reserve and transit time in Moyamoya patients using MRI. *J Cereb Blood Flow Metab*. 2022;43:138-151. doi:10.1177/0271678X221140343
199. Zhao MY, Fan AP, Chen DYT, et al. Using arterial spin labeling to measure cerebrovascular reactivity in Moyamoya disease: insights from simultaneous PET/MRI. *J Cereb Blood Flow Metab*. 2022;42:1493-1506. doi:10.1177/0271678X221083471
200. Wolf RL, Wang J, Detre JA, Zager EL, Hurst RW. Arteriovenous shunt visualization in arteriovenous malformations

- with arterial spin-labeling MR imaging. *Am J Neuroradiol*. 2008;29:681-687. doi:10.3174/ajnr.A0901
201. Zaharchuk G, Bammer R, Straka M, et al. Arterial spin-label imaging in patients with Normal bolus perfusion-weighted MR imaging findings: pilot identification of the Borderzone sign. *Radiology*. 2009;252:797-807. doi:10.1148/radiol.2523082018
 202. Dai W, Fong T, Jones RN, et al. Effects of arterial transit delay on cerebral blood flow quantification using arterial spin labeling in an elderly cohort. *J Magn Reson Imaging*. 2017;45:472-481. doi:10.1002/jmri.25367
 203. Harms MP, Somerville LH, Ances BM, et al. Extending the human connectome project across ages: imaging protocols for the lifespan development and aging projects. *Neuroimage*. 2018;183:972-984. doi:10.1016/j.neuroimage.2018.09.060
 204. ADNI. MRI Scanner Protocols. <https://adni.loni.usc.edu/methods/documents/mri-protocols/> Accessed June 21, 2023.
 205. van der Thiel M, Rodriguez C, Van De Ville D, Gianakopoulos P, Haller S. Regional cerebral perfusion and cerebrovascular reactivity in elderly controls with subtle cognitive deficits. *Front Aging Neurosci*. 2019;11:19. doi:10.3389/fnagi.2019.00019
 206. Mak HKF, Chan Q, Zhang Z, et al. Quantitative assessment of cerebral hemodynamic parameters by QUASAR arterial spin labeling in Alzheimer's disease and cognitively Normal elderly adults at 3-tesla. *J Alzheimers Dis*. 2012;31:33-44. doi:10.3233/JAD-2012-111877
 207. Al-Bachari S, Parkes LM, Vidyasagar R, et al. Arterial spin labelling reveals prolonged arterial arrival time in idiopathic Parkinson's disease. *NeuroImage Clin*. 2014;6:1-8. doi:10.1016/j.nicl.2014.07.014
 208. Paling D, Thade Petersen E, Tozer DJ, et al. Cerebral arterial bolus arrival time is prolonged in multiple sclerosis and associated with disability. *J Cereb Blood Flow Metab*. 2014;34:34-42. doi:10.1038/jcbfm.2013.161
 209. Wang J, Alsop DC, Song HK, et al. Arterial transit time imaging with flow encoding arterial spin tagging (FEAST). *Magn Reson Med*. 2003;50:599-607. doi:10.1002/mrm.10559
 210. Mutsaerts HJ, Petr J, Václavů L, et al. The spatial coefficient of variation in arterial spin labeling cerebral blood flow images. *J Cereb Blood Flow Metab*. 2017;271678X16683690;37:3184-3192. doi:10.1177/0271678X16683690
 211. Cebeci H, Aydin O, Ozturk-Isik E, et al. Assessment of perfusion in glial tumors with arterial spin labeling; comparison with dynamic susceptibility contrast method. *Eur J Radiol*. 2014;83:1914-1919. doi:10.1016/j.ejrad.2014.07.002
 212. Wang L, Wei L, Wang J, et al. Evaluation of perfusion MRI value for tumor progression assessment after glioma radiotherapy: a systematic review and meta-analysis. *Medicine (Baltimore)*. 2020;99:e23766. doi:10.1097/MD.00000000000023766
 213. Furtner J, Schöpf V, Schewzow K, et al. Arterial spin-labeling assessment of normalized vascular Intratumoral signal intensity as a predictor of histologic Grade of astrocytic neoplasms. *Am J Neuroradiol*. 2014;35:482-489. doi:10.3174/ajnr.A3705
 214. Yang S, Zhao B, Wang G, et al. Improving the grading accuracy of astrocytic neoplasms noninvasively by combining timing information with cerebral blood flow: a multi-TI arterial spin-labeling MR imaging study. *Am J Neuroradiol*. 2016;37:2209-2216. doi:10.3174/ajnr.A4907

How to cite this article: Woods JG, Achten E, Asllani I, et al. Recommendations for quantitative cerebral perfusion MRI using multi-timepoint arterial spin labeling: Acquisition, quantification, and clinical applications. *Magn Reson Med*. 2024;92:469-495. doi: 10.1002/mrm.30091